The Astrophysical Journal, 619:503–516, 2005 January 20

ON THE SOFT EXCESS IN THE X-RAY SPECTRUM OF CIRCINUS X-1: REVISITATION OF THE DISTANCE TO CIRCINUS X-1

R. Iaria,[1] M. Spanò,[1] T. Di Salvo,[1] N. R. Robba,[1] L. Burderi,[1,2] R. Fender,[3] M. van der Klis,[3] and F. Frontera[4,5]

Received 2004 July 13; accepted 2004 October 2

ABSTRACT

We report on a 300 ks *BeppoSAX* (0.12–200 keV) observation of Circinus X-1 (Cir X-1) at phases between 0.62 and 0.84 and on a 90 ks *BeppoSAX* observation of Cir X-1 at phases 0.11–0.16. Using the canonical model adopted until now to fit the energy spectrum of this source, large residuals appear below 1 keV. These are well fitted using an equivalent hydrogen column of 0.66×10^{22} cm^{-2}, adding absorption edges of O VII, O VIII, and Ne IX in the spectra extracted from the observation at phases 0.62–0.84 and adding absorption edges of O VII, O VIII, Mg XI, and Mg XII and absorption lines of O VIII and Mg XII in the spectra extracted from the observation at phases 0.11–0.16. During the observation at phases 0.62–0.84 the electron density associated with the ionized matter is $\sim 10^{13}$ cm^{-3}, remaining quite constant going away from the compact object. During the observation at phases 0.11–0.16, the electron density profile varies along the distance going from $\sim 6 \times 10^{13}$ cm^{-3} at $\sim 10^{11}$ cm to $\sim 9 \times 10^{10}$ cm^{-3} at $\sim 10^{13}$ cm. The equivalent hydrogen column toward Cir X-1 is 3 times lower than the value obtained from previous models. This low value would imply that Cir X-1 is at a distance of 4.1 kpc.

Subject headings: accretion, accretion disks — stars: individual (Circinus X-1) — stars: neutron — X-rays: binaries — X-rays: stars

1. INTRODUCTION

Cir X-1 is a peculiar low-mass X-ray binary (LMXB) that recently showed ultrarelativistic outflows similar to those produced by active galactic nuclei (Fender et al. 2004). Because of its rapid variability, a black hole was supposed to be the compact object in this system (Toor 1977) until type I X-ray bursts were detected (Tennant et al. 1986a, 1986b), suggesting that the compact object is a neutron star.

Until 2002 Cir X-1 was supposed to be a runaway binary because of its supposed association with the supernova remnant G321.9-0.3 (Clark et al. 1975) at a distance between 5.5 and 6.5 kpc (Case & Bhattacharya 1998; Stewart et al. 1993). However, the work of Mignani et al. (2002), using *Hubble Space Telescope* (*HST*) data, excluded the association of Cir X-1 with G321.9-0.3. This brings us to a new debate about the distance to Cir X-1. From the observed 21 cm absorption features in the radio spectrum of the source a lower limit to the distance of 6.4–8 kpc was obtained (Goss & Mebold 1977; Glass 1994). Generally in LMXBs the companion star has a mass $\lesssim 1\ M_{\odot}$ and the orbit is almost circular; contrarily, the canonical scenario accepted for Cir X-1 argues that the source has a companion star of ~ 3–$5\ M_{\odot}$ (probably a subgiant; see Johnston et al. 1999), an orbital period of $\sim$16.6 days, deduced from the radio and X-ray light curve of the source, and an eccentric orbit with $e \sim 0.7$–0.9 (Murdin et al. 1980; Tauris et al. 1999).

The correlated spectral and fast-timing properties of accreting low magnetic neutron stars allow us to separate them into two classes, Z and atoll sources, using the pattern each source describes in an X-ray color-color diagram (Hasinger & van der Klis 1989). The Z sources are very bright and could have a moderate magnetic field ($<10^{10}$ G), while the atoll sources have a lower luminosity and probably a weaker magnetic field. The timing analysis of *RXTE* data (Shirey et al. 1996) evidenced that Cir X-1 is more similar to LMXBs of the Z class. However, no quasi-periodic oscillations at kilohertz frequencies were observed in Cir X-1 (Shirey et al. 1996), unlike all the other Z sources.

Cir X-1 also shows a peculiar X-ray spectrum. Brandt et al. (1996), using *ASCA* GIS data taken in 1994 August, found a sudden variation (in a timescale of $\sim$20 minutes) of the flux at phase just after zero, where the count rate increased from $\sim$30 to $\sim$300 counts s^{-1}. In the low count rate state they obtained a good fit to the 0.6–10 keV spectrum of Cir X-1 using a partial covering component, in addition to a two-blackbody model, with a corresponding hydrogen column of $\sim 10^{24}$ cm^{-2} and an intrinsic absorption of $\sim 1.7 \times 10^{22}$ cm^{-2}; in the high count rate state the partial covering of the X-ray spectrum was not needed. Because of the similarity to the spectra of Seyfert 2 galaxies with Compton thin tori, Brandt et al. (1996) suggested that matter at the outer edge of the accretion disk, together with an edge-on disk orientation, could explain the partial covering of the spectrum of Cir X-1 (see, however, Fender et al. 2004).

Iaria et al. (2001a, 2002), using *BeppoSAX* data, analyzed the 0.1–100 keV spectrum of Cir X-1 at phases 0.11–0.16 and 0.61–0.63. They found that the continuum could be described well by a Comptonization model at phases 0.11–0.16 and by the combination of a blackbody plus a Comptonization model at phases 0.61–0.63; the blackbody component is probably produced in the inner region of the accretion disk, while the Comptonized component is produced by a (hotter) corona surrounding the neutron star. A hard excess, dominating the spectrum at energies higher than 15 keV, was also observed in both the observations

[1] Dipartimento di Scienze Fisiche ed Astronomiche, Università di Palermo, Via Archirafi 36, 90123 Palermo, Italy; iaria@gifco.fisica.unipa.it.
[2] Osservatorio Astronomico di Roma, Via Frascati 33, 00040 Monteporzio Catone (Rome), Italy.
[3] Astronomical Institute "Anton Pannekoek," University of Amsterdam and Center for High-Energy Astrophysics, Kruislaan 403, NL 1098 SJ Amsterdam, Netherlands.
[4] Dipartimento di Fisica, Università degli Studi di Ferrara, Via Paradiso 12, I-44100 Ferrara, Italy.
[5] Istituto Astrofisica Spaziale e Fisica Cosmica, CNR, Via Gobetti 101, I-40129 Bologna, Italy.

and fitted by a power-law or a bremsstrahlung component. A similar feature was observed in other Z sources (GX 17+2, Di Salvo et al. 2000; GX 349+2, Di Salvo et al. 2001; GX 5−1, Asai et al. 1994; Sco X-1, D'Amico et al. 2001; Cyg X-2, Di Salvo et al. 2002), suggesting that Cir X-1 shows a behavior similar to that of other Z sources. Finally, a strong absorption edge at ∼8.4–8.7 keV, produced by highly ionized iron, was needed to fit the spectrum of Cir X-1 at phases 0.11–0.16.

The presence of a hard power-law component was recently confirmed by *RXTE* (3–200 keV) observations of Cir X-1 (Ding et al. 2003). They extracted the source spectra at different positions in the color-color diagram and concluded that there is no clear relation between the position of the source in the color-color diagram and the presence of the hard tail in the energy spectrum. An absorption edge, with energy ranging from 8.3 to 9.2 keV, was again observed, together with a localized emission feature present around 10 keV in the energy spectra corresponding to the normal branch and flaring branch; a similar feature was observed by Shirey et al. (1999). They interpret this line as produced by heavy elements, such as nickel, or, less probably, as a blueshifted iron line due to the motion in a relativistic jet or to the rotation of the accretion disk; however, extreme conditions would be required to boost the line energy up to 10 keV in this case.

Iaria et al. (2001b), using *ASCA* data, studied the energy spectrum of Cir X-1 along its orbit. They distinguished three different X-ray states of the source as a function of its phase. Therefore, it was possible to study the evolution of the absorption edge along the orbit of Cir X-1. At the phase of the flaring activity, near phase zero, the hydrogen column derived from the edge was $\sim 10^{24}$ cm^{-2}; at larger values of the phase the hydrogen column decreased; the absorption edge (from ionized iron) was no longer detected at phases from 0.78 to 1, while at these phases a partial covering component was required with an equivalent hydrogen column of $\sim 10^{24}$ cm^{-2}.

In general the X-ray spectrum of Cir X-1 is quite rich with discrete features. Brandt & Schulz (2000), using *Chandra* data, observed Cir X-1 near phase zero. They found P Cygni profiles of lines emitted by highly ionized elements. The outflow velocity necessary to explain the P Cygni profiles was ∼2000 km s^{-1}. Under the hypothesis that the source is seen nearly edge-on, they supposed that the model of a thermally driven wind (Begelman et al. 1983) could explain this outflow of ionized matter from the system. In addition, they suggested that the absorption edge observed by Iaria et al. (2001a) could be connected to the outflow.

The main point that should be clarified is the cycle of 16.6 days observed in the radio and X-ray light curve that was supposed to be the orbital period of the source. Just before phase zero, associated with the radio outbursts, a dip is present in the X-ray folded light curve that was associated with the eclipse of the emitting source by the companion star. The long-term variability of the X-ray light curve and the large flaring activity, present near phase zero, led us to the conclusion that Cir X-1 has an elliptical orbit with a large value of its eccentricity (Murdin et al. 1980) and that phase zero corresponds to the periastron of the orbit. As noted by Clarkson et al. (2004), the dips are near coincident with the presumed periastron passage, suggesting that the semimajor axis of the binary orbit would have to be almost aligned with our line of sight to the binary system, requiring an improbable fine-tuning. Parkinson et al. (2003), studying the *RXTE* all-sky monitor (ASM) light curve of Cir X-1, noted that the periodicity of 16.6 days is not always observed. They analyzed the data from 1996 January 6 to 2002 September 19, finding that the cycle of 16.6 days is not present in a temporal interval lasting 270 days and that in this interval a new weak periodicity of 40 days is observed. If the cycle of 16.6 days is the orbital period of Cir X-1, it is not easy to explain why during around 16 orbital periods the periodicity is no more observed while a new periodicity of 40 days appears. Then the results reported by Parkinson et al. (2003) and Clarkson et al. (2004) seem to indicate that the cycle of 16.6 days is not connected to the orbital period of the binary system. Recently, from three radio observations, Fender et al. (2004) resolved the structure of a jet in Cir X-1. The jet is extended up to 2.″5 from the core. The authors, assuming a distance to the source of 6.5 kpc, found a superluminal motion of the jet having an apparent velocity of $v_{\rm app} \simeq 15c$; because of the large value of the apparent velocity, the angle between the line of sight and the direction of the jet, θ, is $<5^\circ$ and the intrinsic velocity of the jet is $\beta > 0.998$. The detection of the superluminal motion in the jet of Cir X-1 implies that $\theta < 5^\circ$, and since the jet should have a direction almost perpendicular to the accretion disk, it implies that Cir X-1 could not be an edge-on source, contrarily to what was supposed until now.

In this work we assume the ephemeris as reported by Stewart et al. (1991). We present the results of the analysis of the broadband (0.12–200 keV) spectra of Cir X-1 from a *BeppoSAX* observation taken at phases 0.62–0.84 in 2001 September and the reanalysis of the broadband spectrum of Cir X-1 from a previous *BeppoSAX* observation taken at phases 0.11–0.16 in 1998 August (see Iaria et al. 2001a). We note that, although the model used in that paper fitted well the data in the broad energy band 0.1–200 keV, a small bump in the residuals below 1 keV was present (see Fig. 3 in Iaria et al. 2001a). We show that to fit well the data below 1 keV we need to add absorption edges of H-like and He-like ions of oxygen, neon, and magnesium confirming the presence of highly ionized matter around the system. Moreover, we discuss the possibility that Cir X-1 is distant (4.1 kpc), implying that it does not show a super-Eddington luminosity as supposed until now.

The *BeppoSAX* observation of Cir X-1 at phases 0.61–0.63, already published by Iaria et al. (2002) and cited below in the text, is not reanalyzed because the available energy range for the spectral study is 1.8–200 keV, not allowing us to study the spectrum below 1 keV.

2. OBSERVATIONS

Two pointed observations of Cir X-1 were carried out in 2001 between September 08 00:47:57 UT and September 11 07:34:26 UT and on 1998 August 1 15:59:54.5 UT (the latter observation was already analyzed by Iaria et al. 2001a). The total exposure time was, respectively, 115 and 90 ks with the Narrow Field Instruments (NFIs) on board *BeppoSAX* (Boella et al. 1997). These consist of four co-aligned instruments covering the 0.1–200 keV energy range: a Low-Energy Concentrator Spectrometer (LECS; operating in the range 0.1–10 keV), two Medium-Energy Concentrator Spectrometers (MECS; 1.3–10 keV), a High-Pressure Gas Scintillation Proportional Counter (HPGSPC; 7–60 keV), and a Phoswich Detector System (PDS; 13–200 keV). We selected data from the LECS and MECS images in circular regions centered on the source with 8′ and 4′ radius, respectively. Data extracted from the same detector region during blank-field observations were used for background subtraction. The background subtraction for the high-energy (nonimaging) instruments was obtained by using off-source data for the PDS and Earth occultation data for the HPGSPC. Assuming the ephemeris as reported by Stewart et al. (1991), the

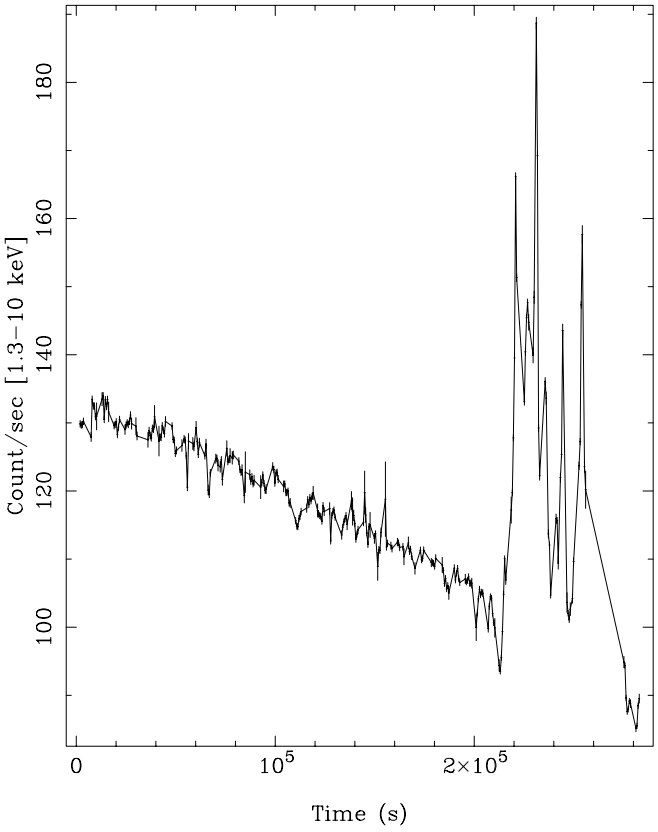

FIG. 1.—Cir X-1 light curve in the energy band 1.3–10 keV (MECS data). The data correspond to the phase interval 0.62–0.84 assuming the ephemeris as reported by Stewart et al. (1991). The bin time is 550 s.

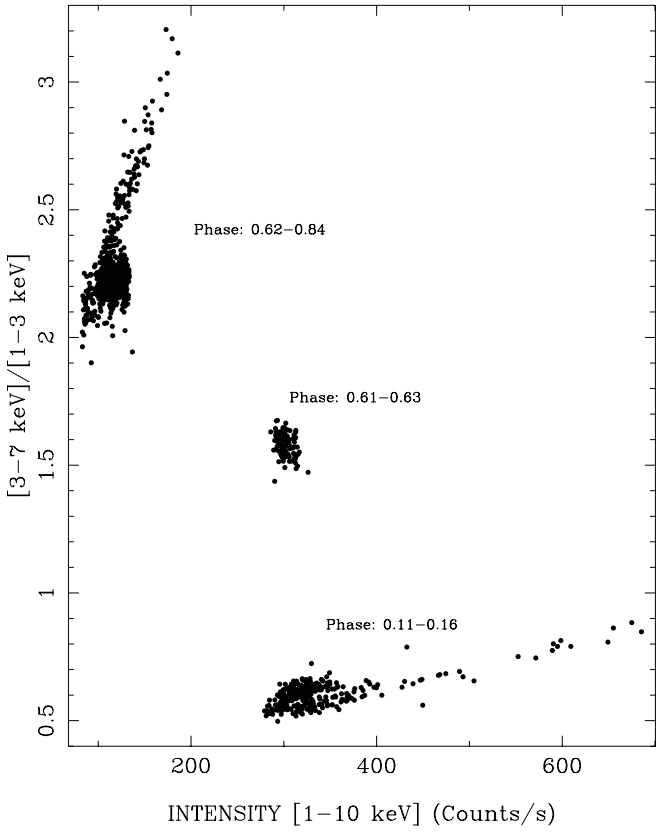

FIG. 2.—Hardness-intensity diagram of Cir X-1. We show in the same box the data at phases 0.11–0.16 (Iaria et al. 2001a), the data at phases 0.61–0.63 (Iaria et al. 2002), and the data at phases 0.62–0.84 (this paper). The bin time is 137 s.

first observation covers the phase interval 0.62–0.84 and the second observation covers the phase interval 0.11–0.16.

In Figure 1 we plot the light curve of the observation at the phase interval 0.62–0.84 in the energy band 1.3–10 keV. The count rate smoothly decreases from ~130 counts s^{-1}, at the beginning of the observation, to ~100 counts s^{-1}, at 210 ks from the beginning of the observation. A flaring episode, lasting 50 ks, is present between 210 and 260 ks from the start time, the count rate varying from ~100 to ~190 counts s^{-1}. The light curve of the observation in the interval phase 0.11–0.16 shows a large flare at the beginning of the observation lasting around 10 ks, and the count rate increases from 300 to ~700 counts s^{-1}; after the flare the count rate varies in a range between 290 and 400 counts s^{-1} (see Fig. 1 in Iaria et al. 2001a).

In Figure 2 we plot the hardness-intensity diagram, where the hardness ratio is the ratio between the count rate in the 3–7 keV energy band and the count rate in the 1–3 keV energy band, and the intensity is the count rate in the 1–10 keV energy band. In this figure we show the data of the two observations of this paper together with those of a previous *BeppoSAX* observation at phase interval 0.61–0.63 (see Iaria et al. 2002) taken in 1999 February. The data of the observation at the phase interval 0.62–0.84 show a lower mean intensity of ~120 counts s^{-1} and a larger hardness ratio than the data taken during the previous observation in the phase interval 0.61–0.63, which shows a count rate of ~300 counts s^{-1}, implying a decrease of the flux by ~60%. In Figure 3 we plot the color-color diagram (CD), where the hard color (HC) is the ratio between the count rate in the energy band 7–10 keV and that in the energy band 3–7 keV and the soft color (SC) is the hardness ratio used for the hardness-intensity diagram. The data at phases 0.62–0.84 are

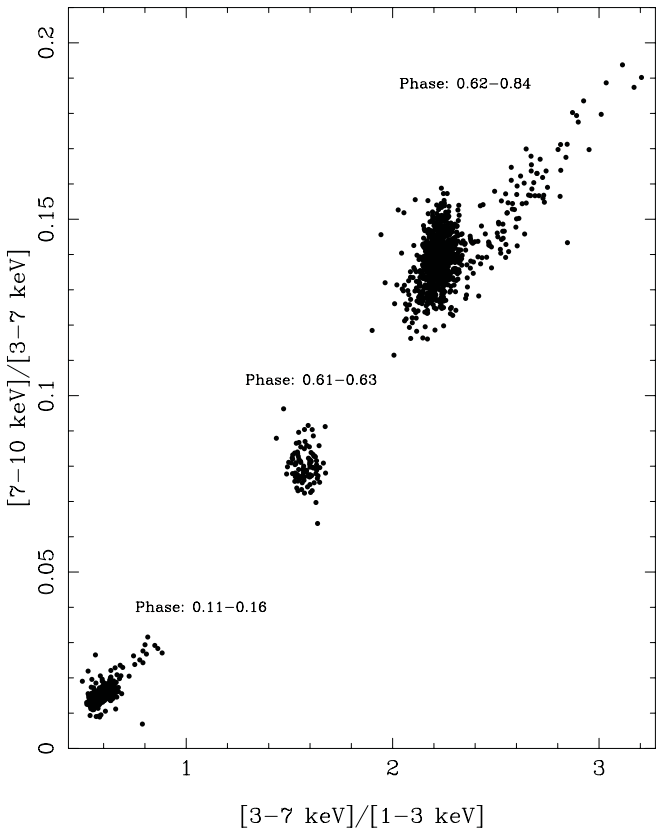

FIG. 3.—Color-color diagram of Cir X-1 of all the *BeppoSAX* observations (same as in Fig. 2). The bin time is 137 s.

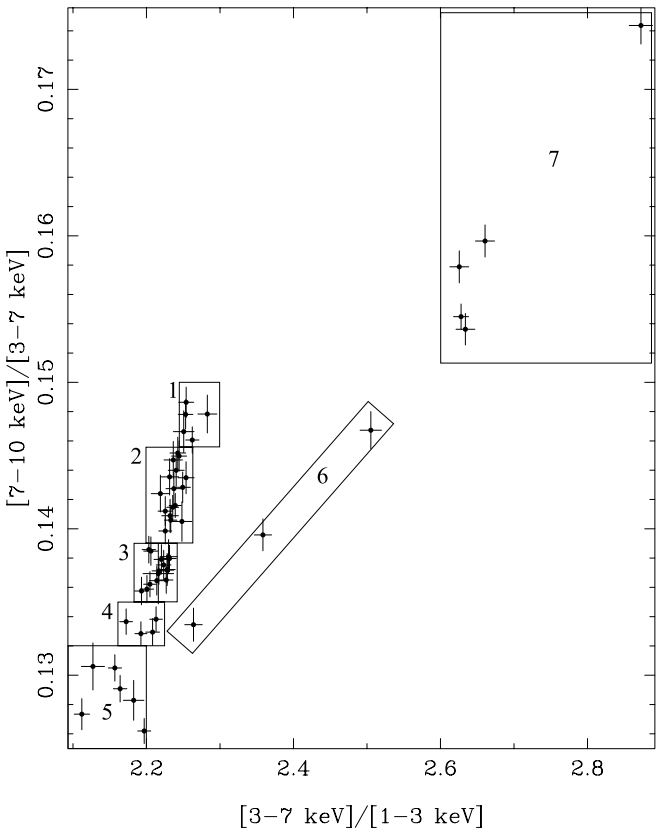

FIG. 4.—Color-color diagram of Cir X-1 corresponding to the observation at phases 0.62–0.84. The boxes indicate the seven selected zones from which we extracted the corresponding energy spectra. The bin time is 5 ks.

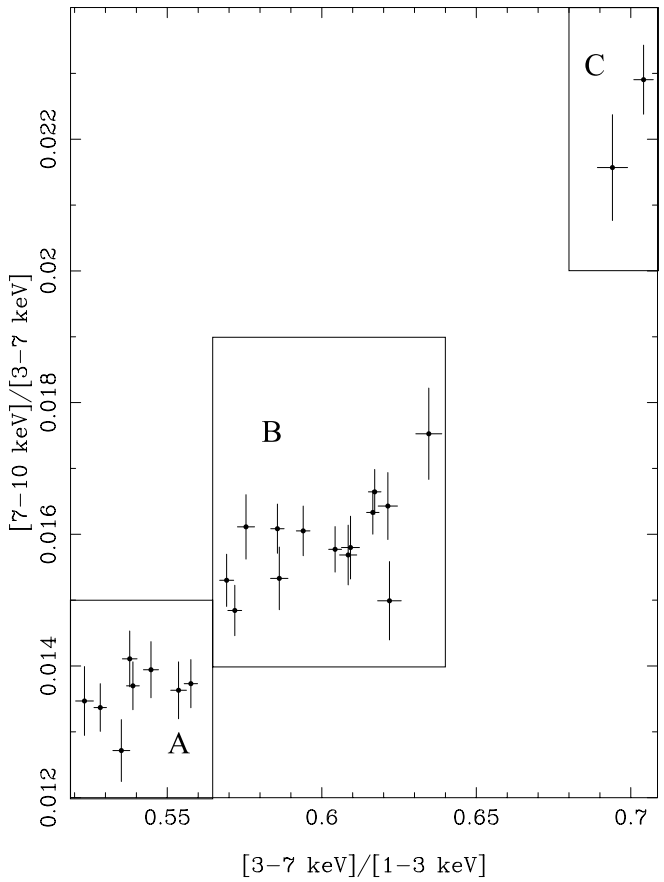

FIG. 5.—Color-color diagram of Cir X-1 corresponding to the observation at phases 0.11–0.16. The boxes indicate the selected regions from which we extracted the corresponding energy spectra. The bin time is 3 ks.

at the top right in this figure, while the data of the previous *BeppoSAX* observation at phases 0.61–0.63 show lower values of both the hard and the soft color. The CD indicates that the spectrum of Cir X-1, in the energy band 1–10 keV, is harder than those corresponding to the previous *BeppoSAX* observations.

To better see this long-term variation, we checked the light curve of Cir X-1 taken by the ASM on board *RXTE*. During the previous observation at phases 0.61–0.63 (start time: 51,216.14 MJD; stop time: 51,217.80 MJD) the corresponding ASM count rate is $\sim$86 counts s^{-1}, while during the observation analyzed here it is $\sim$36 counts s^{-1}, implying that the flux decreased by 58%, in agreement with our *BeppoSAX* observations.

3. SPECTRAL ANALYSIS

In Figure 4 we plot the CD of the observation corresponding to the phase interval 0.62–0.84. A bin time of 5 ks was adopted.

TABLE 1
BeppoSAX OBSERVATION AT PHASES 0.62–0.84

Zone	SC Interval	HC Interval	LECS (ks)	MECS (ks)	HPGSPC (ks)	PDS (ks)
1.....	2.24–2.30	0.145–0.15	4.7	8.7	7.0	3.4
2.....	2.20–2.26	0.139–0.145	7.7	32.0	28.3	14.1
3.....	2.18–2.24	0.135–0.139	9.7	32.1	47.6	14.9
4.....	2.16–2.22	0.132–0.135	2.0	8.9	8.8	4.3
5.....	2.08–2.2	0.124–0.132	1.9	11.9	11.4	4.7
6.....	2.24–2.26	0.124–0.176	1.9	5.1	4.0	1.4
7.....	2.6–2.9	0.124–0.176	4.8	10.5	8.6	9.9

NOTES.—In the second and third columns we show the intervals of soft color (SC) and hard color (HC) that identify the seven zones selected in the CD. In the other columns the corresponding exposure time for each instrument is shown.

The seven zones used to extract the corresponding energy spectra are indicated in the figure; zones 6 and 7 correspond to the flaring episode. In Table 1 we report the intervals of SC and HC that identify the seven selected zones, as well as the exposure times for each of the instruments. For each of the selected zones in the CD we extracted energy spectra for each instrument, which were rebinned in order to have at least 25 counts per energy channel and to oversample the instrumental energy resolution with the same number of channels at all energies.[6] A systematic error of 1% was added to the data. As customary, in the spectral fitting procedure we allowed for a different normalization of the LECS, HPGSPC, and PDS spectra relative to the MECS spectrum, always checking that the derived values are in the standard range for each instrument. The energy ranges used for the spectral analysis are 0.12–4 keV for the LECS, 1.8–10 keV for the MECS, 7–30 keV for the HPGSPC, and 15–200 keV for the PDS. We indicate the seven spectra with numbers from 1 to 7 corresponding to the seven selected zones in the CD.

In Figure 5 we plotted the CD of the observation at phases 0.11–0.16. This observation was already studied by Iaria et al. (2001a), who extracted from eight temporal intervals the corresponding energy spectra, grouping the data in order to have at least 20 counts per energy channel. In this paper we apply to the data the logarithmic grouping (in order to oversample to the instrumental energy resolution with the same number of channels at all energies) and a systematic error of 1%, instead of 2% as done in the previous analysis (see, e.g., Frontera et al. 2001).

[6] See the *BeppoSAX* cookbook at http://www.asdc.asi.it/bepposax/software/cookbook.

TABLE 2

BeppoSAX Observation at Phases 0.11–0.16

Zone	SC Interval	HC Interval	LECS (ks)	MECS (ks)	HP (ks)	PDS (ks)
A.....	0.52–0.565	0.012–0.015	2.5	5.0	4.8	5.0
B.....	0.565–0.64	0.014–0.019	1.7	9.8	11.4	11.1
C.....	0.68–0.71	0.02–0.024	0	0.4	1.0	1.0

From the CD we selected three zones (see Fig. 5); zone C corresponds to the flaring episode. In Table 2 we report the intervals of SC and HC that identify the three selected zones, as well as the exposure times for each of the instruments. We extracted energy spectra for each instrument from zones A and B because zone C does not have enough statistics. The spectra were extracted using the procedure described above. The energy ranges used for the spectral analysis are 0.12–2.85 keV for the LECS, 1.8–10 keV for the MECS, 7–30 keV for the HPGSPC, and 15–200 keV for the PDS. We indicate the energy spectra with letters A and B corresponding, respectively, to the selected zones A and B in the CD.

3.1. *The Soft Excess below* 1 keV

To fit the seven spectra corresponding to the observation taken at phases 0.62–0.84, we used the Comptonization model Comptt (Titarchuk 1994), to which we added a blackbody component at low energies in agreement with Iaria et al. (2002), who studied the source at similar phases. This model gave a χ^2/dof of 285/202, 364/200, 330/200, 254/201, 244/199, 249/199, and 256/200, respectively, for spectra 1–7; in Table 3 we show the corresponding best-fit parameters. The equivalent absorption hydrogen column is $\sim 1.7 \times 10^{22}$ cm^{-2}, the blackbody temperature is around 0.55 keV, the seed photon temperature and the electron temperature of the Comptonized component are around 1 and 2.7 keV, respectively, and finally the optical depth, τ, of the Comptonizing cloud is 11. The residuals obtained for the seven spectra are shown in Figure 6. The residuals corresponding to spectra 1, 2, 3, and 7 show a prominent soft excess reaching the maximum at 0.6–0.7 keV. The excess is less evident in spectra 4, 5, and 6, probably because of the lower statistics due to the lower LECS exposure times in these spectra (see Table 1).

To fit spectra A and B (phases 0.11–0.16), we used the model proposed by Iaria et al. (2001a). The fits gave a χ^2/dof of

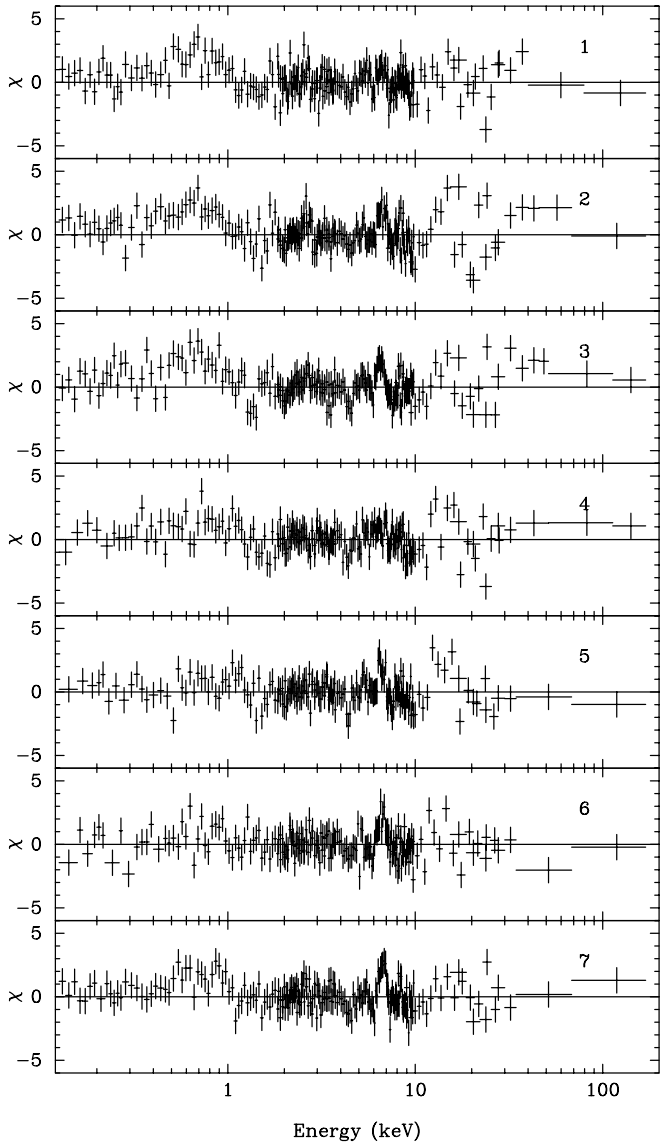

Fig. 6.—Residuals, in units of σ, of the seven spectra corresponding to the observation at phases 0.62–0.84. The residuals are with respect to the model reported in Table 3.

TABLE 3

Results of the Spectral Fits in the 0.12–200 keV Energy Band for the Seven Spectra Corresponding to the Observation Taken at Phases 0.62–0.84

Parameters	1	2	3	4	5	6	7
$N_{\rm H}$ ($\times 10^{22}$ cm^{-2}).....	$1.644^{+0.051}_{-0.049}$	$1.725^{+0.041}_{-0.040}$	$1.703^{+0.037}_{-0.036}$	$1.750^{+0.074}_{-0.070}$	$1.791^{+0.077}_{-0.072}$	$1.730^{+0.077}_{-0.074}$	$1.689^{+0.049}_{-0.048}$
$kT_{\rm BB}$ (keV).....	0.549 ± 0.025	0.531 ± 0.017	0.537 ± 0.015	0.523 ± 0.024	0.505 ± 0.020	0.520 ± 0.022	0.550 ± 0.017
$N_{\rm BB}$ ($\times 10^{-2}$).....	4.67 ± 0.28	4.77 ± 0.18	4.85 ± 0.17	4.87 ± 0.29	4.60 ± 0.26	4.51 ± 0.25	4.68 ± 0.17
kT_0 (keV).....	1.035 ± 0.040	1.034 ± 0.025	1.060 ± 0.023	1.019 ± 0.032	1.040 ± 0.030	1.187 ± 0.037	1.251 ± 0.028
kT_e (keV).....	$2.820^{+0.038}_{-0.035}$	$2.796^{+0.026}_{-0.024}$	$2.725^{+0.026}_{-0.025}$	$2.751^{+0.038}_{-0.036}$	$2.704^{+0.061}_{-0.056}$	$2.678^{+0.091}_{-0.080}$	$2.715^{+0.058}_{-0.052}$
τ	11.93 ± 0.30	11.56 ± 0.21	11.28 ± 0.22	11.36 ± 0.29	10.70 ± 0.39	10.30 ± 0.62	10.43 ± 0.44
$N_{\rm comptt}$.....	1.071 ± 0.041	$1.074^{+0.028}_{-0.027}$	$1.088^{+0.028}_{-0.026}$	$1.127^{+0.040}_{-0.041}$	0.991 ± 0.041	$1.109^{+0.054}_{-0.057}$	$1.256^{+0.039}_{-0.041}$
χ^2 (dof)	285 (202)	364 (200)	330 (200)	254 (201)	244 (199)	249 (199)	256 (200)

Notes.—The photoelectric absorption is indicated as $N_{\rm H}$. The model is composed by a blackbody plus a Comptonized spectrum modeled by Comptt. Uncertainties are at 90% confidence level for a single parameter; upper limits are at 95% confidence level. Parameters $kT_{\rm BB}$ and $N_{\rm BB}$ are, respectively, the blackbody temperature and normalization in units of L_{39}/D_{10}^2, where L_{39} is the luminosity in units of 10^{39} ergs s^{-1} and D_{10} is the distance in units of 10 kpc; kT_0, kT_e, and τ indicate the seed photon temperature, the electron temperature, and the optical depth of the Comptonizing cloud around the neutron star, respectively; and $N_{\rm comptt}$ is the normalization of the Comptt model in XSPEC version 11.2.0 units.

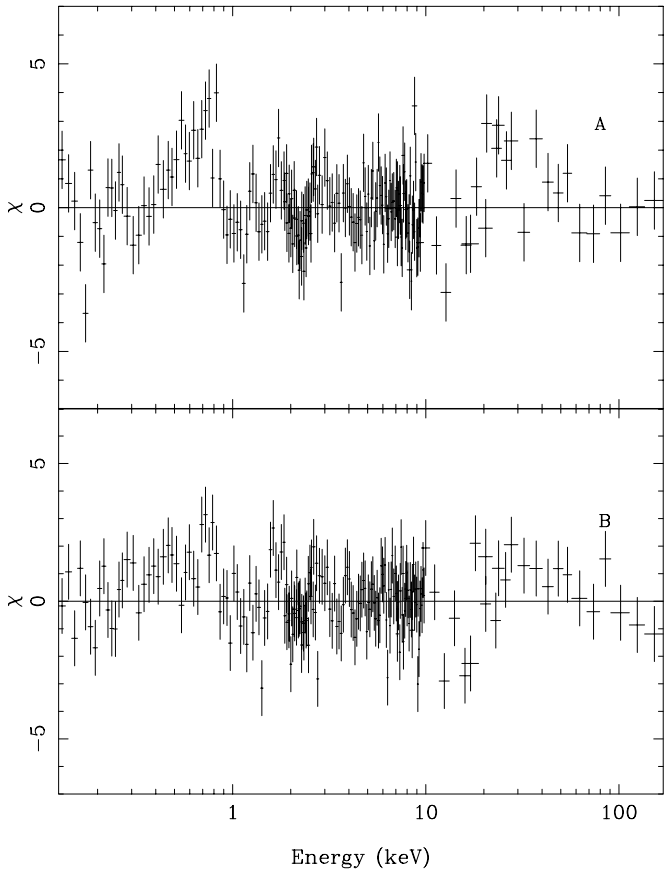

FIG. 7.—Residuals, in units of σ, of spectra A and B corresponding to the observation at phases 0.11–0.16 with respect to the model adopted by Iaria et al. (2001a).

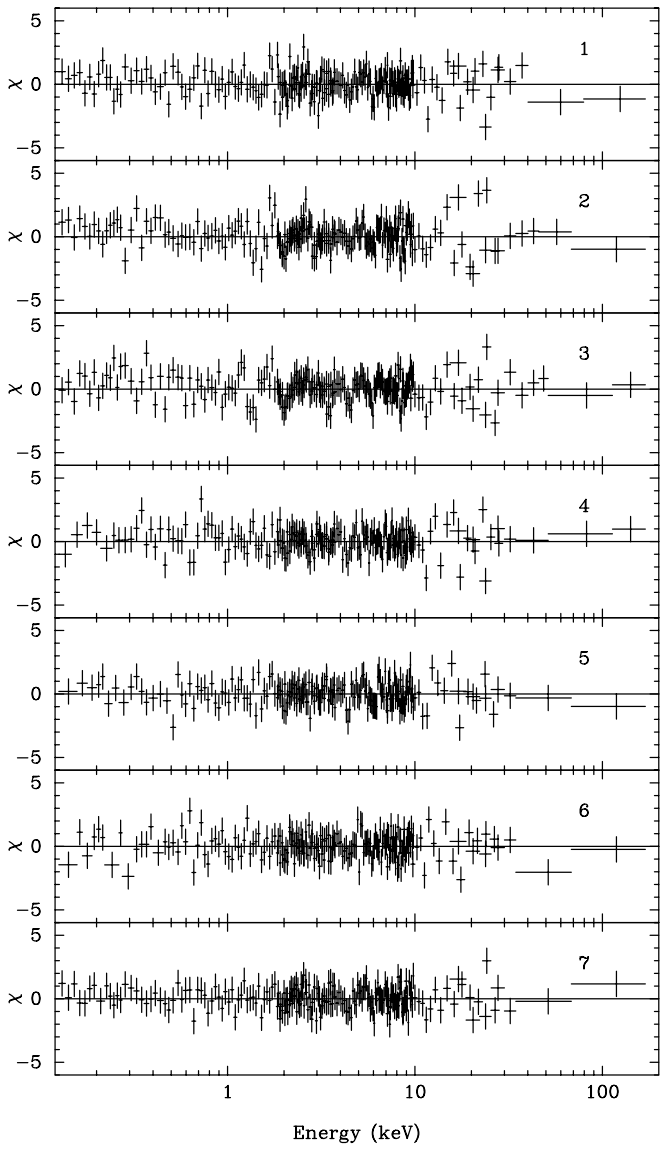

FIG. 8.—Residuals, in units of σ, of the seven spectra corresponding to the observation at phases 0.62–0.84. The residuals are with respect to the model reported in Table 4.

316/176 and 260/175, respectively, for spectrum A and B. The residuals corresponding to the best fits are reported in Figure 7. We note again the presence of a prominent soft excess in the residuals of both spectra reaching the maximum at 0.6–0.7 keV similarly to those obtained from the spectra corresponding to the observation taken at phases 0.62–0.84. This soft excess is less prominent in spectrum B, again probably as a result of the lower statistics due to the lower LECS exposure time in spectrum B (see Table 2).

3.2. *Fitting of the Soft Excess below* 1 keV

To study the soft excess below 1 keV, we start fitting the seven spectra corresponding to the observation taken at phases 0.62–0.84 because of the higher statistics (see Tables 1 and 2). Then we discuss several possible models, and finally we apply the best model to spectra A and B taken at phases 0.11–0.16.

Previous *ASCA* spectra of Cir X-1 were fitted using a partial covering component (Brandt et al. 1996; Iaria et al. 2001b). To compare our results with the previous *ASCA* results, we fitted the seven spectra, in the energy range 1–10 keV, using only LECS and MECS data, with the model reported by Brandt et al. (1996). This model gave a χ^2/dof of 113/124, 119/124, 96/124, 95/124, 94/124, 104/124, and 103/124, respectively, for spectra 1–7. In agreement with Brandt et al. (1996), we find that the continuum emission is well fitted by two blackbody components absorbed by an equivalent hydrogen column of $\sim 1.7 \times 10^{22}$ cm^{-2}. The partial covering component is present in the seven spectra, the equivalent hydrogen column, $N_{\mathrm{H_{pc}}}$, associated with this component is $\sim 2 \times 10^{23}$ cm^{-2}, and the covered fraction of the emitting region is ~ 0.3. We applied the same model to our spectra using the energy range 0.12–10 keV, taking into account the energy range where the soft excess is present. This model gave bad fits with a χ^2/dof of 252/164, 308/164, 373/164, 177/164, 198/164, 198/164, and 204/164, respectively, for spectra 1–7, leaving unchanged the residuals below 1 keV. Finally, we fitted the data in the whole energy range 0.12–200 keV using the continuum emission described in § 3.1, to which we added the partial covering component. We found that the spectrum above 1 keV is well fitted but the soft excess below 1 keV persists, implying that the soft excess cannot be fitted by a partial covering model. These results clearly show that the spectrum of Cir X-1 is more complex than it appeared in the energy band 1–10 keV.

We tried several emission components to fit this soft excess, but none gave reasonable results. The addition of another blackbody component with a temperature of ~ 0.15 keV improved the fit, but the corresponding unabsorbed luminosity was $\sim 10^{42}$ ergs s^{-1} in the 0.1–200 keV energy range. This result

TABLE 4

PARAMETERS OF THE BEST-FIT MODEL IN THE 0.12–200 keV ENERGY BAND FOR THE SEVEN SPECTRA CORRESPONDING TO THE OBSERVATION TAKEN AT PHASES 0.62–0.84

Parameters	1	2	3	4	5	6	7
$N_{\rm H}$ ($\times 10^{22}$ cm^{-2})	0.57 ± 0.12	$0.605^{+0.113}_{-0.085}$	0.67 ± 0.13	0.60 (fixed)	0.60 (fixed)	0.60 (fixed)	$0.45^{+0.16}_{-0.11}$
$E_{\rm edge_1}$ (keV)	$0.697^{+0.044}_{-0.031}$	$0.697^{+0.045}_{-0.032}$	$0.724^{+0.051}_{-0.041}$	$0.680^{+0.046}_{-0.064}$	$0.694^{+0.045}_{-0.079}$	$0.650^{+0.065}_{-0.430}$	$0.659^{+0.044}_{-0.039}$
$\tau_{\rm edge_1}$	5.6 ± 1.6	5.2 ± 1.8	$5.13^{+1.71}_{-0.71}$	$8.0^{+2.9}_{-1.7}$	$7.4^{+2.4}_{-1.5}$	$5.4^{+2.8}_{-2.1}$	$6.3^{+2.9}_{-2.0}$
$E_{\rm edge_2}$ (keV)	1.006 ± 0.079	$0.955^{+0.096}_{-0.074}$	$1.025^{+0.177}_{-0.084}$	1.209 ± 0.078	1.247 ± 0.079	$0.962^{+0.079}_{-0.088}$	0.978 ± 0.053
$\tau_{\rm edge_2}$	$0.90^{+0.78}_{-0.47}$	$1.23^{+1.08}_{-0.78}$	$0.66^{+0.75}_{-0.49}$	$0.38^{+0.20}_{-0.16}$	0.28 ± 0.16	$1.32^{+1.10}_{-0.85}$	$1.30^{+0.67}_{-0.52}$
$E_{\rm Fe\,I}$ (keV)	7.08 ± 0.11	$7.217^{+0.096}_{-0.074}$	$7.127^{+0.093}_{-0.087}$	7.08 ± 0.13	$7.103^{+0.096}_{-0.092}$	7.117 (fixed)	7.117 (fixed)
$\tau_{\rm Fe\,I}$	0.063 ± 0.019	0.056 ± 0.013	0.061 ± 0.013	0.055 ± 0.017	0.076 ± 0.017	0.031 ± 0.029	0.035 ± 0.020
$E_{\rm Fe\,XXV}$ (keV)	9.12 ± 0.21	8.96 ± 0.26	$9.08^{+0.37}_{-0.28}$	8.80 ± 0.18	8.96 ± 0.23	9.04 ± 0.48	$8.91^{+0.28}_{-0.24}$
$\tau_{\rm Fe\,XXV}$	0.053 ± 0.019	0.051 ± 0.013	0.038 ± 0.013	0.064 ± 0.017	0.071 ± 0.019	0.036 ± 0.025	0.038 ± 0.017
$E_{\rm Fe\,XXV}$ (keV)	...	...	...	...	...	$6.67^{+0.20}_{-0.11}$	$6.740^{+0.093}_{-0.051}$
$\sigma_{\rm Fe\,XXV}$ (keV)	...	...	...	...	...	<0.58	<0.23
$I_{\rm Fe\,XXV}$ ($\times 10^{-3}$ photons cm^{-2} s^{-1})	...	...	...	...	...	$4.5^{+2.5}_{-2.1}$	$3.2^{+1.7}_{-1.2}$
$kT_{\rm BB}$ (keV)	$0.642^{+0.048}_{-0.053}$	0.617 ± 0.037	0.611 ± 0.032	0.575 ± 0.052	0.567 ± 0.044	0.561 ± 0.052	0.613 ± 0.038
$N_{\rm BB}$ ($\times 10^{-2}$)	4.58 ± 0.81	$4.26^{+0.54}_{-0.50}$	4.47 ± 0.40	$4.23^{+0.64}_{-0.55}$	$4.06^{+0.40}_{-0.36}$	$3.47^{+0.34}_{-0.39}$	3.82 ± 0.36
kT_0 (keV)	1.14 ± 0.12	$1.099^{+0.073}_{-0.065}$	$1.138^{+0.060}_{-0.055}$	$1.048^{+0.088}_{-0.074}$	$1.090^{+0.077}_{-0.068}$	$1.183^{+0.097}_{-0.084}$	1.295 ± 0.072
kT_e (keV)	$2.709^{+0.075}_{-0.066}$	$2.656^{+0.044}_{-0.041}$	$2.624^{+0.047}_{-0.043}$	$2.608^{+0.063}_{-0.057}$	$2.578^{+0.073}_{-0.067}$	2.58 ± 0.11	2.664 ± 0.090
τ	12.83 ± 0.76	12.69 ± 0.45	12.02 ± 0.45	12.58 ± 0.60	11.79 ± 0.69	11.2 ± 1.1	10.79 ± 0.86
$N_{\rm comptt}$	$1.003^{+0.082}_{-0.077}$	1.028 ± 0.055	1.039 ± 0.048	1.120 ± 0.079	0.974 ± 0.066	$1.121^{+0.083}_{-0.086}$	$1.227^{+0.069}_{-0.076}$
Photon index	2.60 (fixed)	2.60 (fixed)	2.60 (fixed)	2.60 (fixed)	2.60 (fixed)	2.60 (fixed)	2.60 (fixed)
$N_{\rm po}$	0.21 ± 0.15	0.208 ± 0.074	0.180 ± 0.065	0.18 ± 0.12	<0.05	<0.13	<0.16
χ^2 (dof)	203 (193)	246 (191)	222 (191)	189 (193)	182 (191)	198 (189)	161 (189)

NOTES.—The continuum emission is fitted by a blackbody plus a Comptonized component (Comptt) and a power-law component. Uncertainties are at 90% confidence level for a single parameter; upper limits are at 95% confidence level. The power-law normalization, $N_{\rm po}$, is in units of photons keV^{-1} cm^{-2} s^{-1} at 1 keV. $E_{\rm edge_1}$ and $E_{\rm edge_2}$ are the energies of the two absorption edges, $\tau_{\rm edge_1}$ and $\tau_{\rm edge_2}$ their corresponding optical depths (see text). $E_{\rm Fe\,I}$ and $\tau_{\rm Fe\,I}$ are the energy and the corresponding optical depth of the edge associated with neutral iron. $E_{\rm Fe\,XXV}$ and $\tau_{\rm Fe\,XXV}$ are the energy and the corresponding optical depth of the edge associated with Fe XXV. $E_{\rm Fe}$, $\sigma_{\rm Fe\,XXV}$, $I_{\rm Fe\,XXV}$, and EQW$_{\rm Fe\,XXV}$ are, respectively, the centroid, width, intensity, and equivalent width of the emission line at $\sim$6.7 keV. The other parameters are defined as in Table 3.

TABLE 5

PARAMETERS OF THE BEST-FIT MODEL IN THE 0.12–200 keV ENERGY BAND FOR SPECTRA A AND B

Parameters	A	B
$N_{\rm H}$ ($\times 10^{22}$ cm^{-2})	$0.597^{+0.091}_{-0.088}$	$0.621^{+0.140}_{-0.078}$
$E_{\rm edge_1}$ (keV)	$0.624^{+0.042}_{-0.103}$	0.624 (fixed)
$\tau_{\rm edge_1}$	$4.3^{+3.3}_{-1.3}$	3.6 ± 1.7
$E_{\rm edge_2}$ (keV)	$0.824^{+0.039}_{-0.034}$	0.809 ± 0.034
$\tau_{\rm edge_2}$	$2.61^{+0.91}_{-0.97}$	2.60 ± 0.81
$E_{\rm edge_3}$ (keV)	1.352 ± 0.029	1.303 ± 0.045
$\tau_{\rm edge_3}$	$0.145^{+0.048}_{-0.052}$	$0.118^{+0.028}_{-0.053}$
$E_{\rm edge_4}$ (keV)	1.883 ± 0.025	1.870 ± 0.028
$\tau_{\rm edge_4}$	0.128 ± 0.023	$0.122^{+0.024}_{-0.027}$
$E_{\rm Fe\,XXIII}$ (keV)	8.452 ± 0.058	8.467 ± 0.046
$\tau_{\rm Fe\,XXIII}$	$0.809^{+0.109}_{-0.088}$	$0.709^{+0.125}_{-0.081}$
$E_{\rm Fe\,I}$ (keV)	7.117 (fixed)	7.117 (fixed)
$\tau_{\rm Fe\,I}$	<0.070	<0.090
$E_{\rm Fe\,XXV}$ (keV)	6.700 (fixed)	6.700 (fixed)
$\sigma_{\rm Fe\,XXV}$ (keV)	<0.25	<0.61
$I_{\rm Fe\,XXV}$ ($\times 10^{-3}$)	$1.18^{+0.55}_{-0.72}$	$1.86^{+1.42}_{-0.84}$
kT_0 (keV)	$0.416^{+0.018}_{-0.015}$	0.439 ± 0.019
kT_e (keV)	$0.933^{+0.065}_{-0.028}$	$0.997^{+0.091}_{-0.042}$
τ	$14.09^{+0.71}_{-1.37}$	$13.7^{+1.1}_{-1.6}$
$N_{\rm comptt}$	$32.5^{+1.9}_{-4.3}$	$27.3^{+3.6}_{-4.7}$
Photon index	2.60 (fixed)	2.60 (fixed)
$N_{\rm po}$	0.327 ± 0.063	$0.228^{+0.054}_{-0.068}$
χ^2 (dof)	184 (169)	214 (169)

NOTES.—The model is composed of a Comptonized component (Comptt) plus a power-law component. Uncertainties are at 90% confidence level for a single parameter; upper limits are at 95% confidence level. The parameters are defined as in Table 4.

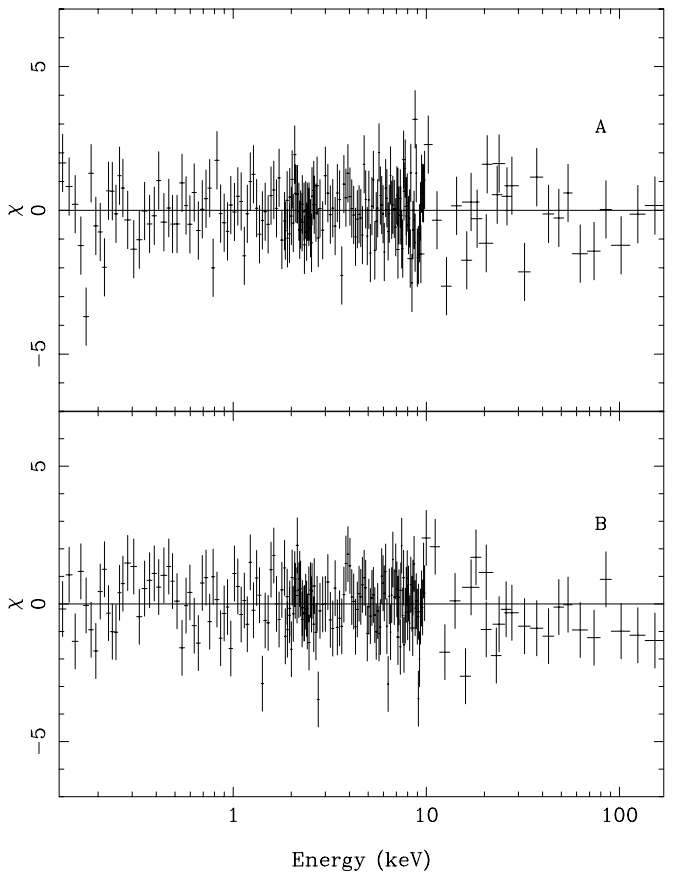

FIG. 9.—Residuals, in units of σ, of spectra A and B corresponding to the observation at phases 0.11–0.16. The residuals are with respect to the model reported in Table 5.

TABLE 6

PARAMETERS OF THE BEST-FIT MODEL IN THE 0.12–200 keV ENERGY BAND FOR THE SEVEN SPECTRA CORRESPONDING TO THE OBSERVATION TAKEN AT PHASES 0.62–0.84

Parameters	1	2	3	4	5	6	7
$N_{\rm H}$ ($\times 10^{22}$ cm^{-2})	0.66 (fixed)	0.66 (fixed)	0.66 (fixed)	0.66 (fixed)	0.66 (fixed)	0.66 (fixed)	0.66 (fixed)
$E_{\rm O\ VII}$ (keV)	0.739 (fixed)	0.739 (fixed)	0.739 (fixed)	0.739 (fixed)	0.739 (fixed)	0.739 (fixed)	0.739 (fixed)
$\tau_{\rm O\ VII}$	$3.20^{+2.13}_{-0.93}$	$3.79^{+2.50}_{-0.93}$	$3.87^{+2.18}_{-0.92}$	$3.0^{+2.9}_{-1.1}$	$5.54^{+0.46}_{-2.38}$	$3.3^{+3.1}_{-1.3}$	$2.39^{+1.23}_{-0.70}$
$E_{\rm O\ VIII}$ (keV)	0.871 (fixed)	0.871 (fixed)	0.871 (fixed)	0.871 (fixed)	0.871 (fixed)	0.871 (fixed)	0.871 (fixed)
$\tau_{\rm O\ VIII}$	$1.63^{+0.57}_{-1.30}$	<2.09	<1.90	<2.41	<1.52	<2.51	$2.05^{+0.48}_{-0.78}$
$E_{\rm Ne\ IX}$ (keV)	1.196 (fixed)	1.196 (fixed)	1.196 (fixed)	1.196 (fixed)	1.196 (fixed)	1.196 (fixed)	1.196 (fixed)
$\tau_{\rm Ne\ IX}$	0.16 ± 0.10	0.126 ± 0.085	0.168 ± 0.074	0.35 ± 0.15	0.31 ± 0.15	<0.17	<0.21
$E_{\rm Fe\ I}$ (keV)	7.117 (fixed)	7.117 (fixed)	7.117 (fixed)	7.117 (fixed)	7.117 (fixed)	7.117 (fixed)	7.117 (fixed)
$\tau_{\rm Fe\ I}$	0.059 ± 0.018	0.052 ± 0.013	0.060 ± 0.013	0.054 ± 0.017	0.077 ± 0.017	0.038 ± 0.027	0.029 ± 0.019
$E_{\rm Fe\ XXV}$ (keV)	9.14 ± 0.21	$8.87^{+0.25}_{-0.20}$	$9.07^{+0.36}_{-0.29}$	8.81 ± 0.17	8.96 ± 0.22	9.02 ± 0.44	$8.91^{+0.29}_{-0.25}$
$\tau_{\rm FeXXV}$	0.050 ± 0.018	0.050 ± 0.012	0.036 ± 0.013	0.061 ± 0.017	0.071 ± 0.019	0.040 ± 0.025	0.036 ± 0.018
$E_{\rm Fe\ XXV}$ (keV)	...	...	...	...	...	6.700 (fixed)	6.700 (fixed)
$\sigma_{\rm Fe\ XXV}$ (keV)	...	...	...	...	...	<0.44	<0.23
$I_{\rm Fe\ XXV}$ ($\times 10^{-3}$)	...	...	...	...	...	$4.2^{+2.3}_{-1.9}$	$3.3^{+1.7}_{-1.3}$
EQW$_{\rm Fe\ XXV}$ (eV)	...	...	...	...	...	30^{+17}_{-13}	19^{+10}_{-7}
$kT_{\rm BB}$ (keV)	$0.623^{+0.049}_{-0.052}$	0.607 ± 0.035	0.604 ± 0.029	0.584 ± 0.048	0.575 ± 0.040	$0.578^{+0.051}_{-0.048}$	0.602 ± 0.037
$N_{\rm BB}$ ($\times 10^{-2}$)	$4.49^{+0.78}_{-0.72}$	$4.36^{+0.48}_{-0.45}$	$4.50^{+0.38}_{-0.35}$	$4.39^{+0.62}_{-0.53}$	4.10 ± 0.39	$3.59^{+0.47}_{-0.40}$	$3.97^{+0.38}_{-0.34}$
$R_{\rm BB}$ (km)	20 ± 5	20 ± 3	21 ± 3	22 ± 5	22 ± 4	20 ± 5	20 ± 3
Flux$_{\rm BB}$ (10^{-8} ergs cm^{-2} s^{-1})	$\sim$0.38	$\sim$0.37	$\sim$0.38	$\sim$0.37	$\sim$0.34	$\sim$0.30	$\sim$0.33
kT_0 (keV)	$1.110^{+0.110}_{-0.094}$	$1.102^{+0.066}_{-0.062}$	$1.138^{+0.055}_{-0.050}$	$1.065^{+0.084}_{-0.070}$	$1.099^{+0.072}_{-0.068}$	$1.207^{+0.096}_{-0.084}$	$1.285^{+0.073}_{-0.065}$
kT_e (keV)	$2.710^{+0.060}_{-0.055}$	2.686 ± 0.039	$2.643^{+0.042}_{-0.040}$	$2.631^{+0.061}_{-0.057}$	$2.580^{+0.071}_{-0.068}$	$2.592^{+0.116}_{-0.094}$	$2.663^{+0.091}_{-0.082}$
τ	12.84 ± 0.63	12.48 ± 0.40	11.86 ± 0.40	12.38 ± 0.58	$11.77^{+0.70}_{-0.66}$	11.0 ± 1.1	$10.82^{+0.79}_{-0.83}$
$N_{\rm comptt}$	1.023 ± 0.076	1.028 ± 0.050	1.038 ± 0.044	$1.100^{+0.071}_{-0.075}$	$0.966^{+0.065}_{-0.062}$	$1.103^{+0.080}_{-0.088}$	$1.237^{+0.065}_{-0.072}$
Flux$_{\rm Comptt}$ (10^{-8} ergs cm^{-2} s^{-1})	$\sim$1.56	$\sim$1.52	$\sim$1.46	$\sim$1.54	$\sim$1.28	$\sim$1.47	$\sim$1.76
R_W (km)	6 ± 1	6 ± 1	6 ± 1	7 ± 1	6 ± 1	6 ± 1	5 ± 1
Photon index	2.60 (fixed)	2.60 (fixed)	2.60 (fixed)	2.60 (fixed)	2.60 (fixed)	2.60 (fixed)	2.60 (fixed)
$N_{\rm po}$	0.19 ± 0.10	0.168 ± 0.061	0.139 ± 0.054	0.12 ± 0.11	<0.044	<0.44	<0.071
Flux$_{\rm po}$ (10^{-8} ergs cm^{-2} s^{-1})	$\sim$0.18	$\sim$0.16	$\sim$0.13	$\sim$0.11	<0.04	<0.41	<0.07
$L_{\rm tot}$ ($\times 10^{37}$ ergs s^{-1})	$\sim$4.3	$\sim$4.1	$\sim$4.0	$\sim$4.1	<3.4	<4.5	<4.3
χ^2 (dof)	210 (196)	254 (194)	224 (194)	187 (195)	182 (193)	205 (191)	176 (192)

NOTES.—The continuum emission is the same as reported in Table 4. The absorption edges at low energies are interpreted as produced by ions of light elements, and their corresponding optical depths are reported. Uncertainties are at 90% confidence level for a single parameter; upper limits are at 95% confidence level. Flux$_{\rm BB}$, Flux$_{\rm Comptt}$, and Flux$_{\rm po}$ are the intrinsic fluxes in the energy band 0.12–200 keV of the blackbody, the Comptonized component, and the power-law component, respectively. $L_{\rm tot}$ is the intrinsic total luminosity in the energy band 0.12–200 keV and assuming a distance to the source of 4.1 kpc.

is very hard to explain assuming that the X-ray binary system contains a neutron star or a Galactic black hole. Instead of a blackbody we added a Gaussian line centered at 0.6 keV. Also in this case the results were not physically acceptable because, owing to the high $N_{\rm H}$, the corresponding equivalent width of the line was larger than 1 keV.

We conclude that the soft excess may have two possible origins: (1) there is a continuum emission component below 1 keV absorbed by a lower value of equivalent hydrogen column with respect to the $N_{\rm H}$ absorbing the spectrum above 1 keV, or (2) the equivalent hydrogen column of the whole spectrum is overestimated.

With regard to the first hypothesis, the residuals below 1 keV disappear if we add to the previous model a continuum emission component absorbed by a different lower equivalent hydrogen column ($N_{\rm H} \sim 8 \times 10^{20}$ cm^{-2}) than that absorbing the other components of the model ($\sim 1.7 \times 10^{22}$ cm^{-2}). However, in this case it is hard to explain the lower value of $N_{\rm H}$ since the emitting source should be less distant than 1 kpc. Because in the LECS and MECS field of view no contaminating source is visible, we should conclude that Cir X-1 is less distant than 1 kpc or that a source with coordinates compatible with those of Cir X-1, at a distance less than 1 kpc, is present. Since this scenario looks unrealistic, in this paper we concentrate on the second hypothesis.

The second hypothesis would imply an equivalent hydrogen column, $N_{\rm H}$, lower than $\sim 1.7 \times 10^{22}$ cm^{-2}. A good fit of the broadband spectra is obtained adding two absorption edges at 0.7 and 1–1.2 keV having a large optical depth of $\sim$5 and $\sim$1, respectively. The threshold energy of the first absorption edge is similar in all seven spectra, while the threshold energy of the second absorption edge varies between 1 and 1.2 keV. Adding these features, we find that the equivalent hydrogen column $N_{\rm H}$ is $\sim 0.6 \times 10^{22}$ cm^{-2} and the spectrum below 1 keV is well fitted.

In the residuals of spectra 2 and 3 a hard excess is present. In agreement with previous works (Iaria et al. 2001a, 2002; Ding et al. 2003), we fitted it adding a power-law component having a photon index fixed to 2.6 in all seven spectra. In spectra 6 and 7 a Gaussian emission line, having its centroid at 6.7 keV, was needed. Two localized features are present at 7 and 9 keV in the seven spectra; we added two absorption edges to fit them. The residuals with respect to the final model are reported in Figure 8, and the best-fit parameters are reported in Table 4.

Because the structure of the residuals below 1 keV is the same in the spectra of both the observations presented in this work, we fitted spectra A and B, corresponding to the observation taken at phases 0.11–0.16, adding two absorption edges at 0.6 and 0.8 keV, in the model adopted by Iaria et al. (2001a). In this case the fits are improved adding two further absorption edges at 1.3 and 1.9 keV.

The parameters of these fits are reported in Table 5, and the residuals corresponding to the best fits are plotted in Figure 9. The addition of four absorption edges does not significantly change the parameters associated with the Comptonized component and the power-law component. The photon index of the

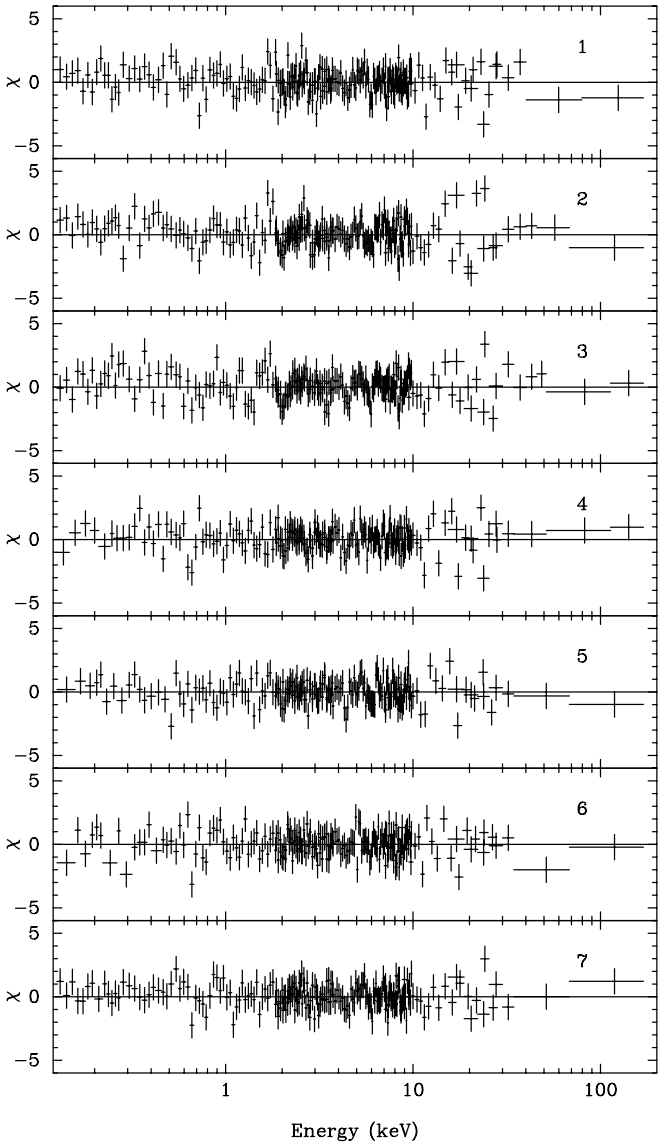

FIG. 10.—Residuals, in units of σ, of the seven spectra corresponding to the observation at phases 0.62–0.84. The residuals are with respect to the model reported in Table 6.

TABLE 7

PARAMETERS OF THE BEST-FIT MODEL IN THE 0.12–200 keV ENERGY BAND FOR SPECTRA A AND B

Parameters	A	B
$N_{\rm H}$ ($\times 10^{22}$ cm^{-2})	0.66 (fixed)	0.66 (fixed)
$E_{\rm O\ VII}$ (keV)	0.739 (fixed)	0.739 (fixed)
$\tau_{\rm O\ VII}$	$4.22^{+1.07}_{-0.58}$	$4.17^{+1.10}_{-0.67}$
$E_{\rm O\ VIII}$ (keV)	0.871 (fixed)	0.871 (fixed)
$\tau_{\rm O\ VIII}$	$0.76^{+0.43}_{-0.62}$	<1.08
$E_{\rm Mg\ XI}$ (keV)	1.762 (fixed)	1.762 (fixed)
$\tau_{\rm Mg\ XI}$	$0.103^{+0.090}_{-0.038}$	0.104 ± 0.36
$E_{\rm Mg\ XII}$ (keV)	1.963 (fixed)	1.963 (fixed)
$\tau_{\rm Mg\ XII}$	$0.052^{+0.059}_{-0.017}$	0.048 ± 0.017
$E_{\rm Fe\ I}$ (keV)	7.117 (fixed)	7.117 (fixed)
$\tau_{\rm Fe\ I}$	<0.094	<0.089
$E_{\rm edge_1}$ (keV)	8.447 ± 0.057	8.464 ± 0.041
$\tau_{\rm edge_1}$	$0.84^{+0.12}_{-0.10}$	$0.732^{+0.093}_{-0.080}$
$E_{\rm O\ VIII}$ (keV)	0.6537 (fixed)	0.6537 (fixed)
$\sigma_{\rm O\ VIII}$ (keV)	<0.34	<0.06
$I_{\rm O\ VIII}$	-1.36 ± 0.27	$-1.24^{+0.29}_{-0.35}$
EQW$_{\rm O\ VIII}$ (eV)	-125 ± 25	-135^{+33}_{-37}
$E_{\rm Mg\ XII}$ (keV)	1.4726 (fixed)	1.4726 (fixed)
$\sigma_{\rm Mg\ XII}$ (keV)	<0.18	<0.08
$I_{\rm Mg\ XII}$	$-0.171^{+0.075}_{-0.610}$	$-0.140^{+0.050}_{-0.097}$
EQW$_{\rm Mg\ XII}$ (eV)	-19^{+8}_{-69}	-17^{+6}_{-12}
$E_{\rm Fe\ XXIII}$ (keV)	6.62 (fixed)	6.62 (fixed)
$\sigma_{\rm Fe\ XXIII}$ (keV)	<0.31	0.31 (fixed)
$I_{\rm Fe\ XXIII}$ ($\times 10^{-3}$)	$1.12^{+0.64}_{-0.74}$	$1.75^{+0.81}_{-0.89}$
EQW$_{\rm Fe\ XXIII}$ (eV)	29^{+18}_{-20}	39 ± 20
kT_0 (keV)	$0.430^{+0.015}_{-0.035}$	0.447 ± 0.014
kT_e (keV)	$0.959^{+0.083}_{-0.052}$	$1.018^{+0.080}_{-0.054}$
τ	$13.5^{+1.2}_{-1.6}$	$13.2^{+1.9}_{-3.0}$
$N_{\rm comptt}$	$29.5^{+2.8}_{-3.9}$	$25.9^{+1.9}_{-3.0}$
Flux$_{\rm Comptt}$ (10^{-8} ergs cm^{-2} s^{-1})	$\sim$4.9	$\sim$4.8
R_W (km)	100 ± 20	90 ± 10
Photon index	2.60 (fixed)	2.60 (fixed)
$N_{\rm po}$	0.322 ± 0.065	$0.219^{+0.055}_{-0.064}$
Flux$_{\rm po}$ (10^{-8} ergs cm^{-2} s^{-1})	$\sim$0.30	$\sim$0.21
$L_{\rm tot}$ ($\times 10^{38}$)	$\sim$1.0	$\sim$1.0
χ^2 (dof)	187 (170)	207 (170)

NOTES.—The model is defined in Table 5. We fixed the energies of the absorption edges present at low energies, finding the corresponding optical depths. Uncertainties are at 90% confidence level for a single parameter; upper limits are at 95% confidence level.

power law is fixed to 2.6 (as in spectra 1–7). The equivalent hydrogen column is $\sim 0.6 \times 10^{22}$ cm^{-2}, compatible with the values obtained from the other observation.

The poor LECS energy resolution and the low statistics below 1 keV do not allow us to identify well the absorption features at low energies. For this reason we fit spectra 1–7 fixing the equivalent hydrogen column to 0.66×10^{22} cm^{-2} and the threshold energies of the absorption edges to those of O VII, O VIII, and Ne IX. We use the same continuum model reported in Table 4. In Table 6 we report the best-fit parameters, and in Figure 10 we show the residuals with respect to this model. We note that the parameters of the continuum components are unchanged and that we obtain good fits for all seven spectra. Finally, we fit spectra A and B also fixing the equivalent hydrogen column to 0.66×10^{22} cm^{-2} and the threshold energies of the absorption edges to those of O VII, O VIII, Mg XI, and Mg XII. In this case two Gaussian absorption lines associated with O VIII and Mg XII are added at $\sim$0.65 and $\sim$1.47 keV, respectively. Also in this case we find good fits, and the best-fit parameters of the continuum are unchanged with respect to the model reported in Table 5; the new results are reported in Table 7, and the residuals are plotted in Figure 11.

4. DISCUSSION

We analyzed data of Cir X-1 from two *BeppoSAX* observations taken in 2001 September and 1998 August at phases 0.62–0.84 and 0.11–0.16, respectively.

About the observation at phases 0.62–0.84, taken in 2001, the light curve, the hardness-intensity diagram, and the color-color diagram show that the intensity has decreased and soft and hard colors have increased with respect to previous observations at similar phases (0.61–0.63; Iaria et al. 2002). We selected seven zones in the color-color diagram and extracted from each of them the corresponding spectrum. The spectra, in the energy band 1–10 keV, are similar to those of other Z sources (see Di Salvo et al. 2000, 2001; Iaria et al. 2004) and are well fitted by a blackbody and a Comptonized component. Below 1 keV a soft excess is present in the residuals of spectra 1, 2, 3, and 7 (see Fig. 6); this can be fitted adding two absorption edges at 0.7 and 1 keV. The equivalent hydrogen

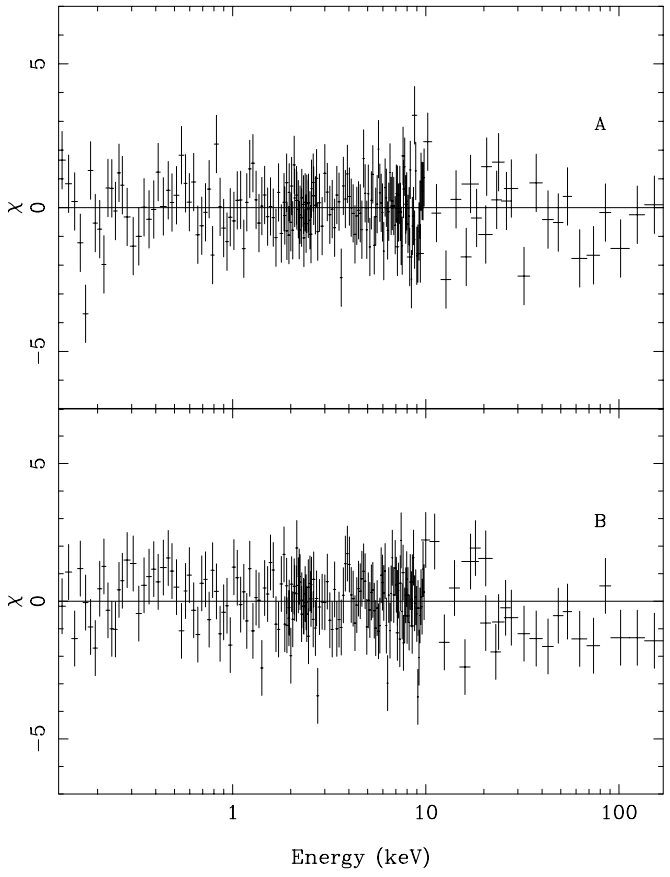

FIG. 11.—Residuals, in units of σ, of the two spectra corresponding to the observation at phases 0.11–0.16. The residuals are with respect to the model reported in Table 7.

column density, $N_{\rm H}$, absorbing the continuum emission is $\sim 0.6 \times 10^{22}$ cm^{-2}. In spectra 4, 5, and 6, where the soft excess is not evident, we fixed $N_{\rm H}$ to 0.6×10^{22} cm^{-2} and added two absorption edges at low energies, obtaining similar results. For this reason we conclude that in these spectra the absence of the soft excess below 1 keV is due to the lower statistics in the LECS data (see Table 1). However, the poor LECS energy resolution and the low statistics below 1 keV do not allow us to identify well the absorption features at low energies. For this reason we fitted spectra 1–7 fixing the equivalent hydrogen column to 0.66×10^{22} cm^{-2} and the threshold energies of the absorption edges to those of O VII, O VIII, and Ne IX. In the following we discuss the latter model.

About the observation at phases 0.11–0.16 taken in 1998, we reanalyzed data already published by Iaria et al. (2001a), extracting the spectra from the corresponding color-color diagram, while in the previous paper the spectra were extracted from eight temporal intervals along the entire observation. This provides evidence of the soft excess below 1 keV, only marginally visible in the previous analysis (see Fig. 3 in Iaria et al. 2001a). The continuum used to fit the data and the corresponding best-fit parameters are the same as reported by Iaria et al. (2001a). The addition of four absorption edges at 0.6, 0.8, 1.3, and 1.9 keV changes the equivalent absorption column so that it is now $\sim 0.6 \times 10^{22}$ cm^{-2} instead of $\sim 1.7 \times 10^{22}$ cm^{-2} as reported in the previous paper. Also in this analysis, a prominent absorption edge at 8.4 keV and a Gaussian line at $\sim$6.7 keV are present as already discussed by Iaria et al. (2001a). In addition, for this observation the poor LECS energy resolution and the low statistics below 1 keV do not allow us to identify well the absorption features at low energies. For this reason we fitted spectra A and B fixing the equivalent hydrogen column to 0.66×10^{22} cm^{-2} and the threshold energies of the absorption edges to those of O VII, O VIII, Mg XI, and Mg XII. In this case two Gaussian absorption lines associated with O VIII and Mg XII are added at $\sim$0.65 and $\sim$1.47 keV, respectively. In the following we discuss the latter model.

This modeling was possible thanks to the good spectral coverage of the *BeppoSAX* LECS, which gives us the ability to study the X-ray spectrum down to 0.1 keV. For instance, recent *Chandra* observations (Brandt & Schulz 2000; Schulz & Brandt 2002) did not allow adequate determination of the continuum and the absorption features below 1 keV because the useful spectral range was limited to 1.4–7.3 keV. On the other hand, a K-shell absorption edge of neutral iron was observed in the two *Chandra* observations, although the choice to fix the hydrogen absorption column to 2×10^{22} cm^{-2} might have influenced the value of the optical depth of the edge obtained from the fit. In a previous *ASCA* observation (Brandt et al. 1996) the estimated equivalent hydrogen column was $N_{\rm H} \sim 1.7 \times 10^{22}$ cm^{-2}, similar to the value that we found not including the absorption edges at low energies (see Table 3). Note that the *ASCA* energy band used by Brandt et al. (1996) is 1–10 keV, which does not allow a clear detection of possible absorption edges at 0.7–1 keV. We confirm their results in the energy range 1–10 keV, where the spectrum is well fitted with an $N_{\rm H} \sim 1.7 \times 10^{22}$ cm^{-2} and where the K-shell absorption edge associated with neutral iron is fitted using a partial covering component. However, extending the energy range down to 0.1 keV, this model does not fit the data below 1 keV.

4.1. *The Distance to Cir X-1*

A source having the position of Cir X-1 and a distance of 5.5 kpc (Case & Bhattacharya 1998) has a corresponding visual extinction of 5.8 ± 2.0 mag (Hakkila et al. 1997) and, using the observed correlation between visual extinction and equivalent hydrogen column (Predehl & Schmitt 1995), an equivalent hydrogen column $N_{\rm H} = (1.03 \pm 0.02) \times 10^{22}$ cm^{-2}. In the previous *ASCA* (Brandt et al. 1996; Iaria et al. 2001b) and *BeppoSAX* (Iaria et al. 2001a, 2002) observations an equivalent absorption column of $\sim 1.7 \times 10^{22}$ cm^{-2} was found, and the authors concluded that an excess of obscuring matter was present close to the X-ray source. The value of the $N_{\rm H}$ obtained in this analysis is smaller than the previous one by a factor of 3. The absorption we find (Tables 4 and 5) implies that for a source having the position of Cir X-1 the corresponding distance should be around 4 kpc.

If the interpretation of our data is correct, the debate about the distance of Cir X-1 now becomes complicated. The $N_{\rm H}$-based distance is not compatible with a distance of 6.4–8 kpc obtained from the 21 cm absorption features in the radio spectrum of the source (Goss & Mebold 1977; Glass 1994). Now we discuss this result using the latest estimate of the distance $R_0 = 8.5 \pm 0.5$ kpc of the Galactic center from the Sun (Feast & Whitelock 1997) obtained using *Hipparcos* data.

Looking at the absorption H I spectrum in the direction of Cir X-1 (see Fig. 1 in Goss & Mebold 1977), we see that five prominent radial velocities are present at 3.0, -6.5, -21.0, -57.5, and -75 km s^{-1} with a resolution of 0.82 km s^{-1}; the latter feature extends down to -90 km s^{-1}. Goss & Mebold (1977) observed in the direction of Cir X-1 seven times. The first observation was done when Cir X-1 was supposed not emitting in the radio band (spectrum 1) while three radio spectra, corresponding to three distinct observations, were averaged when the radio flux

TABLE 8
RADIAL VELOCITIES AND OTHER PARAMETERS

v_r (km s^{-1}) (1)	R (kpc) (2)	d (kpc) (3)	A_v (mag) (4)	$N_{\rm H}$ (cm^{-2}) (5)	μ (mas yr^{-1}) (6)
−75.0	5.3 ± 0.3	5.9 ± 0.8	$6.4^{+3.0}_{-2.5}$	1.14 ± 0.21	0.4 ± 0.5
		7.6 ± 0.8	$8.9^{+3.9}_{-3.2}$	1.59 ± 0.24	-0.3 ± 0.3
−57.5	5.8 ± 0.4	4.1 ± 0.3	3.7 ± 1.4	0.66 ± 0.09	1.4 ± 0.3
		9.3 ± 0.6	$11.4^{+4.3}_{-3.7}$	2.04 ± 0.20	-0.6 ± 0.2
−21	7.8 ± 0.5	0.9 ± 0.1	0.73 ± 0.35	0.130 ± 0.005	5.5 ± 1.0
		12.5 ± 0.7	$16.1^{+6.4}_{-5.5}$	2.88 ± 0.23	-0.39 ± 0.06
−6.5	8.1 ± 0.5	0.5 ± 0.1	$0.50^{+0.35}_{-0.30}$	0.090 ± 0.016	3.3 ± 1.0
		12.9 ± 0.8	$16.7^{+6.9}_{-5.9}$	2.98 ± 0.26	-0.13 ± 0.02
3.0	8.6 ± 0.5	13.6 ± 0.8	$17.7^{+7.6}_{-6.3}$	3.17 ± 0.27	0.06 ± 0.02

NOTES.—Col. (1): Radial velocities corresponding to the absorption features present in the H I spectrum of Cir X-1 (see Goss & Mebold 1977). Col. (2): Radius of the orbit of the clouds along the line of sight. Col. (3): Corresponding distances to the clouds of neutral matter. Cols. (4) and (5): Visual extinction and equivalent hydrogen column corresponding to the distances. Col. (6): Proper motion of the clouds. These values are calculated assuming a distance to the Galactic center of 8.5 ± 0.5 kpc (Feast & Whitelock 1997). The velocity at 3 km s^{-1} gives only one value of d because its orbit has a radius larger than 8.5 kpc (see text).

of Cir X-1 was around 1 Jy; spectrum 1 was subtracted from the averaged spectrum. Supposing that no contaminating variable radio sources were present during the observations, the absorption line corresponding to the farthest H I cloud gives a lower limit to the distance to Cir X-1. Goss & Mebold (1977), assuming a distance to the center of our Galaxy $R_0 = 10$ kpc and looking toward the direction of Cir X-1 at $l = 322.^{\circ}117$ and $b = 0.^{\circ}038$, obtained that the minimum distance between the Galactic center and the tangential point $R = R_0 \sin l$ is 6.1 kpc and that the distance to the tangential point $d = R_0 \cos l$ is 7.9 kpc. At the tangential point the radial velocity will be maximum, in our case $v_r = -88 \pm 1$ km s^{-1} (see Fig. 2 in Rohlfs et al. 1986). Since the radial velocity at -75 km s^{-1} extends up to -90 km s^{-1} and since -90 km s^{-1} is compatible with the radial velocity at the tangential point, they assumed $d = 7.9$ kpc as a lower limit to the distance to Cir X-1. Rescaling these results using the most recent estimation of the distance to the Galactic center $R_0 = 8.5 \pm 0.5$ (Feast & Whitelock, 1997), the lower limit to the distance of Cir X-1 should be $d = 6.7 \pm 0.4$ kpc. However, we note that (1) although the radial velocity at -75 km s^{-1} extends down to -90 km s^{-1}, the associated optical depth drastically decreases below 1 at -76 km s^{-1}, becoming less prominent in the absorption line at 3 km s^{-1} (see Fig. 1 in Goss & Mebold 1977); and (2) the absorption line at 3 km s^{-1} is produced by a cloud having a distance larger than the distance to the tangential point, implying that the lower limit to the Cir X-1 distance should be larger (>13 kpc; see Table 8) than that actually accepted. Note that the corresponding equivalent hydrogen column associated with a distance of 13 kpc is $\sim 3 \times 10^{22}$ cm^{-2}, never observed in the X-ray spectra of Cir X-1. This suggests that possible contaminating radio sources are present during the observation. For these reasons we analyzed all the absorption lines present in the H I spectrum. To do it, we used

$$v_r = W(R) \sin l \cos b$$

and

$$R^2 = R_0^2 + d^2 - 2R_0 d \cos l$$

(see Olling & Merrifield 1998 and references therein). The function $W(R)$ is defined as $W(R) = R_0[\Omega(R) - \Omega_0(R_0)]$, where $\Omega(R)$ is the angular speed of a celestial body around the Galactic center, R is the radius of the circular orbit, and $\Omega_0(R_0)$ is the angular speed of the local standard of rest (LSR). Using the method of the tangential point, it is possible to write the function $W(R)$ as a function of R (see Fig. 2 in Merrifield 1992 and references therein); solving the two equations above, we find the distances reported in Table 8.

In order to discriminate between these values, we computed the corresponding visual extinction (Hakkila et al. 1997), the equivalent hydrogen column (Predehl & Schmitt 1995), and the proper motion μ (not corrected for the solar motion) for each distance. These values are also reported in Table 8. Excluding the distances of 0.5 and 0.9 kpc, because the corresponding $N_{\rm H}$ value is lower than that observed in the X-ray spectra of Cir X-1, we can give $d = 4.1 \pm 0.3$ kpc as a lower limit to the distance of Cir X-1. On the other hand, we can exclude the distances 12.5, 12.9, and 13.6 kpc because the corresponding $N_{\rm H}$ values are larger than those observed in the X-ray spectra of Cir X-1. Using this argument, the distance of the source should be in the range between 4.1 ± 0.3 and 9.3 ± 0.6 kpc. Our conclusion is in agreement with the results of $d > 4$ kpc obtained by Whelan et al. (1977) using data in the optical band. Finally, we note that (1) a recent *HST* observation of the optical counterpart of Cir X-1 indicates that its proper motion (not corrected for the solar motion) is $\mu = 1.5 \pm 1.6$ mas yr^{-1} (Mignani et al. 2002), similar to the proper motion obtained for the lower limit of $d = 4.1 \pm 0.3$ kpc (see Table 8); and (2) the value of $N_{\rm H}$ that we obtain from the fit in this work is around 0.6×10^{22} cm^{-2} (see Tables 4 and 5), compatible with the value of $N_{\rm H}$ obtained for $d = 4.1 \pm 0.3$ kpc. For this reason, in the following we adopt a distance to Cir X-1 of 4.1 kpc, and the corresponding value of $N_{\rm H}$ is 0.66×10^{22} cm^{-2} (see Table 8), the same fixed in the fits reported in Tables 6 and 7.

This value of distance to Cir X-1 slightly changes the parameters associated with the radio jet observed from the source (Fender et al. 2004). From three radio observations Fender et al. (2004) resolved the structure of a jet in Cir X-1; the jet is extended up to $2.''5$ from the core. The authors, assuming a distance to the source of 6.5 kpc, find a superluminal motion of the jet with an apparent velocity of $v_{\rm app} \simeq 15c$; because of the large value of the apparent velocity, the angle between the line of sight and the direction of the jet, θ, is $<5^{\circ}$ and the intrinsic

velocity of the jet is $\beta > 0.998$. For a distance to Cir X-1 of 4.1 kpc, as we suggest, these values slightly change because now $v_{\rm app} \simeq 9.2c$, implying $\theta < 12^\circ$ and $\beta > 0.995$. The extension of the jet of 2.″5 corresponds to 0.12 lt-yr for 4.1 kpc, i.e., 1.1×10^{17} cm. The detection of the superluminal motion in the jet of Cir X-1 implies $\theta < 12^\circ$, and since the jet should have a direction almost perpendicular to the accretion disk, it confirms that Cir X-1 is not an edge-on source.

In light of these results, the mechanism producing the P Cygni profiles from strongly ionized elements, observed by Brandt & Schulz (2000) using a *Chandra* observation, should be reanalyzed. The authors proposed a radiatively driven wind along the disk surface to explain the presence of these features in the *Chandra* grating spectra (for more details about their proposed model see Brandt & Schulz 2000; Schulz & Brandt 2002), but this mechanism could be valid only assuming that Cir X-1 is an edge-on source.

A possibility that should be investigated is that the ionized matter is ejected in a nearly perpendicular direction to the accretion disk surface.

4.2. *The Absorption Features in the Spectra and Possible Reflection*

In this section we discuss the absorption features reported in Tables 6 and 7 and obtained fixing the value of $N_{\rm H}$ to 0.66×10^{22} cm^{-2}.

For spectra 1–7 the absorption edges associated with O VII, O VIII, and Ne IX are probably produced in a plasma having an ionization parameter $\log_{10}\xi \sim 1.3$; for this value of ξ the fractional number f of O VII, O VIII, and Ne IX of the corresponding elements is largest. We obtain the equivalent hydrogen column corresponding to the optical depth of the absorption edges using $\tau_{\rm X} = \sigma_{\rm X} N_{\rm H} A_{\rm X} f$, where $\sigma_{\rm X}$ is the photoionization cross section for the ion X, $N_{\rm H}$ is the corresponding equivalent hydrogen column, $A_{\rm X}$ is the abundance of the element X, and f is the fractional number of ions in the given ionization state of the considered element. The values of the photoionization cross sections are 2.4×10^{-19}, 9.9×10^{-20}, and 1.5×10^{-19} cm^2 for O VII, O VIII, and Ne IX, respectively (see Verner et al. 1996). Using the values of τ reported in Table 6, as well as the cosmic abundance of oxygen and neon, and assuming an ionization parameter of $\log_{10}\xi = 1.3$ (implying $f \sim 0.5$ for O VII, O VIII, and Ne IX), we find that $N_{\rm H_{O\ VII}} \sim 3 \times 10^{22}$ cm^{-2}, $N_{\rm H_{O\ VIII}} \sim 4 \times 10^{22}$ cm^{-2}, and $N_{\rm H_{Ne\ IX}} \sim 2 \times 10^{22}$ cm^{-2}. We also observe an absorption edge probably associated with Fe XXV at 9 keV. The photoionization cross section of Fe XXV is 2.0×10^{-20} cm^2 (see Verner et al. 1996). Assuming an ionization parameter $\log_{10}\xi$ of 3.3 (which implies the largest value of $f \sim 0.65$), we obtain that $N_{\rm H_{Fe\ XXV}}$ is $\sim 8.3 \times 10^{22}$ cm^{-2}. In spectra 6 and 7 an emission line associated with Fe XXV is present. From $\xi = L_{\rm X}/n_e r^2$ (see Krolik et al. 1981) and $L_{\rm line} = 4\pi D^2 I_{\rm line} = n_e^2 V \alpha A f$, we can obtain the distance, r, from the central source and the corresponding electron density, n_e, of the region where the line is produced. In the formulae $L_{\rm X}$ is the total unabsorbed X-ray luminosity of the source in the energy band 0.12–200 keV, $L_{\rm line}$ is the luminosity of the line, D is the distance to the source, $I_{\rm line}$ is the intensity of the line, V is the emitting volume, α is the recombination parameter, and A is the cosmic abundance of iron. We assume a spherical volume V of radius r, and, as written above, $\log_{10}\xi = 3.3$ implies $f \sim 0.65$. The recombination parameter α is obtained using the relation and the best-fit parameters for H-like and He-like ions reported by Verner & Ferland (1996), where we fixed the plasma temperature at the electron temperature of the Comptonizing cloud; we find that the Fe XXV line is produced at $r \sim 2 \times 10^{10}$ cm, with a corresponding electron density of $n_e \sim 7 \times 10^{13}$ cm^{-3}. We can also estimate an upper limit to the distance to the emitting source, d, of the region where the absorption edges are produced. To do it, we use $d < L_{\rm X}/(N\xi)$ (Reynolds & Fabian 1995), where N is the equivalent hydrogen column associated with the photoionized matter, d is the distance to the central object, and ξ and $L_{\rm X}$ are defined as above. We find that the O VII, O VIII, and Ne IX absorption edges are produced at a distance to the central object of $d < 5.3 \times 10^{13}$ cm, and the Fe XXV absorption edge at $d < 2.5 \times 10^{11}$ cm. The latter distance is compatible with the distance associated with the Fe XXV absorption line.

In spectra A and B we fixed four absorption edges below 2 keV. The absorption edges associated with O VII and O VIII should be produced in a region having a lower ionization parameter (we assume $\log_{10}\xi = 1$) with respect to the region where the absorption edges of Mg XI and Mg XII are produced (we assume $\log_{10}\xi = 2.2$ for the latter region). For spectra A and B we use a lower value of $\log_{10}\xi = 1$ associated with O VII and O VIII than in spectra 1–7 because now we do not observe the Ne IX absorption edge.

Using the values of τ reported in Table 7, as well as the solar abundance of oxygen, and assuming an ionization parameter $\log_{10}\xi$ of 1 (implying $f \sim 0.5$ for O VII and $f \sim 0.25$ for O VIII), we find that $N_{\rm H_{O\ VII}}$ and $N_{\rm H_{O\ VIII}}$ are $\sim 4 \times 10^{22}$ cm^{-2}. In the same way, knowing that the values of the photoionization cross sections of Mg XI and Mg XII are 1.0×10^{-19} and 4.4×10^{-20} cm^2, respectively (see Verner et al. 1996), and assuming an ionization parameter $\log_{10}\xi$ of 2.2 (which implies the largest values of $f \sim 0.4$ for Mg XI and $f \sim 0.45$ for Mg XII), we obtain that $N_{\rm H_{Mg\ XI}}$ and $N_{\rm H_{Mg\ XII}}$ are $\sim 7 \times 10^{22}$ cm^{-2}. An absorption edge probably associated with Fe XXIII is also present at 8.5 keV. The photoionization cross section of Fe XXIII is 2.2×10^{-20} cm^2 (Krolik & Kallman 1987). Assuming an ionization parameter $\log_{10}\xi$ of 2.9 (which implies the largest value of $f \sim 0.25$), we obtain that $N_{\rm H_{Fe\ XXIV}}$ is $\sim 4 \times 10^{24}$ cm^{-2}, as already proposed by Iaria et al. (2001a). The upper limit to the distance of the region where this absorption edge is produced is $d < 3.3 \times 10^{10}$ cm.

Two absorption lines, associated with O VIII and Mg XII, are present. The ionization parameter $\log_{10}\xi$ associated with O VIII is 1, implying $f \sim 0.25$. We obtain that the O VIII absorption line is produced at $r \sim 1 \times 10^{13}$ cm, with a corresponding electron density of $n_e \sim 9 \times 10^{10}$ cm^{-3}. The ionization parameter $\log_{10}\xi$ associated with Mg XII is 2.2, implying $f \sim 0.45$; we find that the Mg XII absorption line is produced at $r \sim 1 \times 10^{11}$ cm, with a corresponding electron density of $n_e \sim 6.2 \times 10^{13}$ cm^{-3}. On the other hand, we find that the O VII and O VIII absorption edges are produced at $d < 2.5 \times 10^{14}$ cm and the Mg XI and Mg XII absorption edges are produced at $d < 1 \times 10^{13}$ cm. These upper limits are compatible with the distances derived for the O VIII and Mg XII absorption lines.

Finally, an emission line at 6.7 keV is observed. Assuming the hypothesis that this is produced by Fe XXV, we find that the distance and the electron density of the region producing this line are $r \sim 6 \times 10^{11}$ cm and $n_e \sim 1.6 \times 10^{11}$ cm^{-3}, respectively. This result is unrealistic because it implies the presence of plasma with an ionization parameter of $\log_{10}\xi = 3.3$ at a larger distance than the plasma having $\log_{10}\xi = 2.2$, where the Mg XII absorption line is produced. A possible explanation is that the emission line at $\sim$6.7 keV is associated with Fe XXIII; the corresponding centroid of the line should be $\sim$6.62 keV, and this does not change the results of the best fit for spectra A and B. In this case,

TABLE 9

SUMMARY OF THE DISTANCE d, THE ELECTRON DENSITIES n_e, AND THE EQUIVALENT HYDROGEN COLUMN N ASSOCIATED WITH THE IONIZED ELEMENTS

Parameter	O VII Edge	O VIII Edge	O VIII Line	Ne IX Edge	Mg XI Edge	Mg XI Edge	Mg XII Line	Fe XXIII Edge	Fe XXV Line	Fe XXV Edge
Phases 0.62–0.84										
$\log_{10}\xi$.....	1.3	1.3	...	1.3	...	...	...	...	3.3	3.3
f.....	0.5	0.5	...	0.5	...	...	...	...	0.65	0.65
d (cm).....	$<5.3\times10^{13}$	$<5.3\times10^{13}$	...	$<5.3\times10^{13}$	...	...	...	...	$\sim2\times10^{10}$	$<2.5\times10^{11}$
N (cm^{-2})	$\sim3\times10^{22}$	$\sim4\times10^{22}$	...	$\sim2\times10^{22}$	...	...	...	...	...	$\sim8.3\times10^{22}$
n_e (cm^{-3}).....	...	...	...	...	...	...	...	...	$\sim7\times10^{13}$	...
Phases 0.11–0.16										
$\log_{10}\xi$.....	1.0	1.0	1.0	...	2.2	2.2	2.2	2.9	...	...
f.....	0.5	0.25	0.25	...	0.4	0.45	0.45	0.25	...	...
d (cm).....	$<2.5\times10^{14}$	$<2.5\times10^{14}$	$\sim1\times10^{13}$	...	$<1\times10^{13}$	$<1\times10^{13}$	$\sim1\times10^{11}$	$<3.3\times10^{10}$	...	...
N (cm^{-2})	$\sim4\times10^{22}$	$\sim4\times10^{22}$	...	...	$\sim7\times10^{22}$	$\sim7\times10^{22}$	...	$\sim4\times10^{24}$	...	...
n_e (cm^{-3}).....	...	...	$\sim9.2\times10^{10}$	...	...	...	$\sim6.2\times10^{13}$	...	...	...

NOTE.—Parameters f and $\log_{10}\xi$ are defined in the text.

unfortunately, we do not know the recombination parameter of the line and, consequently, we cannot calculate the distance to the region where this line is produced.

Summarizing these results gives the indication that ionized matter is present around the system. During the observation at phases 0.62–0.84, this ionized matter could have an electron density quite constant along the distance of $\sim7\times10^{13}$ cm^{-3}; during the observation at phases 0.11–0.16, the electron density decreases going from the compact object to larger distances, varying between 9×10^{10} cm^{-3} at 1×10^{13} cm and 6×10^{13} cm^{-3} at 1×10^{11} cm. The different distribution of ionized matter along the distance from the neutron star, during the two observations, may influence the different observed continuum emission (see § 4.3). In Table 9 we summarize the obtained results.

Finally, we observe an absorption edge associated with neutral iron in all nine spectra. This feature was also observed during the *Chandra* observations (Brandt & Schulz 2000; Schulz & Brandt 2002). The optical depth is ~0.05 for spectra 1–7 and less than 0.09 for spectra A and B. Knowing that the cross section of the iron K edge is 3.7×10^{-20} cm^2, we find that the equivalent hydrogen column associated with this feature is $N_{\mathrm{H_{Fe\,I}}}\sim3\times10^{22}$ cm^{-2} and $N_{\mathrm{H_{Fe\,I}}}<5\times10^{22}$ cm^{-2} for the observation at phases 0.62–0.84 and 0.11–0.16, respectively. The estimated equivalent hydrogen column associated with the neutral iron is about 5 times higher than seen in the low-energy absorption, indicating an overabundance of iron or special geometrical conditions. A plausible geometry was suggested by Singh & Apparao (1994), who found similar results for the atoll source 4U 0614+09 analyzing *EXOSAT* data. The Fe I absorption edge is imprinted on the spectrum owing to reflection by cold or partially ionized matter that is not in the same line of sight as the direct emission and therefore leads to an estimate of N_{H} that is different from the value obtained from low-energy absorption.

4.3. *The Parameters of the Continuum Emission Components*

The model used to fit the data taken at phases 0.62–0.84 is typical of the Z sources (see Iaria et al. 2004 and references therein). It is composed of a blackbody plus a Comptonized component and a power law at energies above 10 keV. The corresponding radius of the blackbody component, assuming a spherical emission and a distance of 4.1 kpc, is ~20 km. This radius is too large to be associated with the emission from the neutron star surface; therefore, the blackbody component is probably emitted by the inner part of the accretion disk. Following in't Zand et al. (1999), we calculated the radius, R_W, of the seed photon–emitting region using the parameters reported in Table 6 and a distance to the source of 4.1 kpc; we obtain $R_W\sim6$ km, which is smaller than the neutron star radius. A possible implication is that the electron cloud is not spherical. The continuum obtained at phases 0.11–0.16 was already discussed by Iaria et al. (2001a) and is fitted by a very soft Comptonized component plus a power-law component; no blackbody emission is observed. In this case R_W is ~100 km and the shielding of the inner regions could be produced by a optically thicker region of the corona at inner radius. Assuming that the Comptonizing corona produces also the absorption feature observed in the spectra, we deduce that during the observation at phases 0.62–0.84 the ionized matter has a low density, allowing us to observe the inner region of the system up to 20 km from the compact object, while during the observation at phases 0.11–0.16 the density of the ionized matter is highest near the compact object, forming a curtain that does not allow us to observe the inner region.

We also note that although in the two observations considered in this paper the continuum emission below 10 keV is different, the spectra above 10 keV are fitted by a power-law component described by the same parameters, suggesting that its presence is independent of the phase and luminosity of the X-ray source. As described in other works (see Iaria et al. 2004 and references therein), it could be connected to the presence of a motion of relativistic electrons in a jet, as also suggested by Fender et al. (2004; see below).

The intrinsic total luminosity in the energy band 0.12–200 keV, L_{X}, is $\sim4\times10^{37}$ ergs s^{-1} during the observation at phases 0.62–0.84 and $\sim1\times10^{38}$ ergs s^{-1} during the observation at phases 0.11–0.16 for a distance to the source of 4.1 kpc.

5. CONCLUSIONS

In this work we present the analysis of the broadband (0.12–200 keV) spectrum of Cir X-1 at phases 0.62–0.84 and the reanalysis of the broadband (0.12–200 keV) spectrum of Cir X-1 at phases 0.11–0.16, using two *BeppoSAX* observations taken in 2001 and 1998, respectively. In the spectra, a soft excess below 1 keV is observed using the model previously proposed. We fitted the soft excess using the equivalent hydrogen column of 0.66×10^{22} cm^{-2} and adding at low energies absorption edges

of O VII, O VIII, Ne IX, Mg XI, and Mg XII. Moreover, in the observation at phases 0.11–0.16 two absorption lines of O VIII and Mg XII were added.

The equivalent hydrogen column of the interstellar matter of 0.66×10^{22} cm^{-2} gives a distance to Cir X-1 of 4.1 kpc. This result is discussed, comparing it to the values obtained by Goss & Mebold (1977) and reanalyzing the H I spectrum of the source.

We discuss the different continuum observed in the two observations as being due to the different density of the ionized matter around the binary system in the two observations.

Finally, the reader should note that our results could be model dependent; for this reason further spectroscopic analyses of the Cir X-1 spectrum below 1 keV are needed to confirm the scenario proposed in this work.

This work was partially supported by the Italian Space Agency (ASI) and the Ministero della Istruzione, della Universitá, e della Ricerca (MIUR).

REFERENCES

Asai, K., Dotani, T., Mitsuda, K., Nagase, F., Kamado, Y., Kuulkers, E., & Breedon, L. M. 1994, PASJ, 46, 479
Begelman, M. C., McKee, C. F., & Shields, G. A. 1983, ApJ, 271, 70
Boella, G., Butler, R. C., Perola, G. C., Piro, L., Scarsi, L., & Blecker, J. 1997, A&AS, 122, 299
Brandt, W. N., Fabian, A. C., Dotani, T., Nagase, F., Inoue, H., Kotani, T., & Segawa, Y. 1996, MNRAS, 283, 1071
Brandt, W. N., & Schulz, N. S. 2000, ApJ, 544, L123
Case, G. L., & Bhattacharya, D. 1998, ApJ, 504, 761
Clark, D. H., Parkinson, J. H., & Caswell, J. L. 1975, Nature, 254, 674
Clarkson, W. I., Charles, P. A., & Onyett, N. 2004, MNRAS, 348, 458
D'Amico, F., Heindl, W. A., Rothschild, R. E., & Gruber, D. E. 2001, ApJ, 547, L147
Ding, G. Q., Qu, J. L., & Li, T. P. 2003, ApJ, 596, L219
Di Salvo, T., Robba, N. R., Iaria, R., Stella, L., Burderi, L., & Israel, G. L. 2001, ApJ, 554, 49
Di Salvo, T., et al. 2000, ApJ, 544, L119
———. 2002, A&A, 386, 535
Feast, M., & Whitelock, P. 1997, MNRAS, 291, 683
Fender, R., Wu, K., Johnston, H., Tzioumis, T., Jonker, P., Spencer, R., & van der Klis, M. 2004, Nature, 427, 222
Frontera, F., et al. 2001, ApJ, 561, 1006
Glass, I. S. 1994, MNRAS, 268, 742
Goss, W. M., & Mebold, U. 1977, MNRAS, 181, 255
Hakkila, J., Myers, J. M., Stidham, B. J., & Hartmann, D. H. 1997, AJ, 114, 2043
Hasinger, G., & van der Klis, M. 1989, A&A, 225, 79
Iaria, R., Burderi, L., Di Salvo, T., La Barbera, A., & Robba, N. R. 2001a, ApJ, 547, 412
Iaria, R., Di Salvo, T., Burderi, L., & Robba, N. R. 2001b, ApJ, 561, 321
Iaria, R., Di Salvo, T., Robba, N. R., & Burderi, L. 2002, ApJ, 567, 503
———. 2004, ApJ, 600, 358
in't Zand, J. J. M., et al. 1999, A&A, 345, 100
Johnston, H. M., Fender, R., & Wu, K. 1999, MNRAS, 308, 415
Krolik, J. H., & Kallman, T. R., 1987, ApJ, 320, L5
Krolik, J. H., McKee, C. F., & Tarter, C. B. 1981, ApJ, 249, 422
Merrifield, M. R. 1992, AJ, 103, 1552
Mignani, R. P., De Luca, A., Caraveo, P. A., & Mirabel, I. F. 2002, A&A, 386, 487
Murdin, P., Jauncey, D. L., Haynes, R. F., Lerche, I., Nicolson, G. D., Holt, S. S., & Kaluzienski, L. J. 1980, A&A, 87, 292
Olling, R. P., & Merrifield, M. R. 1998, MNRAS, 297, 943
Parkinson, P. M. Saz, et al. 2003, ApJ, 595, 333
Predehl, P., & Schmitt, J. H. M. M. 1995, A&A, 293, 889
Reynolds, C. S., & Fabian, A. C. 1995, MNRAS, 273, 1167
Rohlfs, K., Boehme, R., Chini, R., & Wink, J. E. 1986, A&A, 158, 181
Schulz, N. S., & Brandt, W. N. 2002, ApJ, 572, 971
Shirey, R. E., Bradt, H. V., & Levine, A. M. 1999, ApJ, 517, 472
Shirey, R. E., Bradt, H. V., Levine, A. M., & Morgan, E. H. 1996, ApJ, 469, L21
Singh, K. P., & Apparao, K. M. V. 1994, ApJ, 431, 826
Stewart, R. T., Caswell, J. L., Haynes, R. F., & Nelson, G. J. 1993, MNRAS, 261, 593
Stewart, R. T., Nelson, G. J., Penninx, W., Kitamoto, S., Miyamoto, S., & Nicolson, G. D. 1991, MNRAS, 253, 212
Tauris, T. M., Fender, R. P., van den Heuvel, E. P. J., Johnston, H. M., & Wu, K. 1999, MNRAS, 310, 1165
Tennant, A. F., Fabian, A. C., & Shafer, R. A. 1986a, MNRAS, 219, 871
———. 1986b, MNRAS, 221, 27P
Titarchuk, L. 1994, ApJ, 434, 570
Toor, A. 1977, ApJ, 215, L57
Verner, D. A., & Ferland, G. J. 1996, ApJS, 103, 467
Verner, D. A., Ferland, G. J., Korista, K. T., & Yakovlev, D. G. 1996, ApJ, 465, 487
Whelan, J. A. J., et al. 1977, MNRAS, 181, 259